

1 **Projecting end of century climate extremes and their impacts on the**  
2 **hydrology of a representative California watershed**

3  
4 Fadji Z. Maina<sup>1,3\*</sup>, Alan Rhoades<sup>2</sup>, Erica R. Siirila-Woodburn<sup>1</sup>, Peter-James Dennedy-Frank<sup>1</sup>  
5 <sup>1</sup> Energy Geosciences Division, Lawrence Berkeley National Laboratory 1 Cyclotron Road, M.S.  
6 74R-316C, Berkeley, CA 94704, USA

7 <sup>2</sup> Climate and Ecosystem Sciences Division, Lawrence Berkeley National Laboratory 1  
8 Cyclotron Road, M.S. 74R-316C, Berkeley, CA 94704, USA

9 <sup>3</sup> now at NASA Goddard Space Flight Center, Hydrological Sciences Laboratory, Greenbelt,  
10 MD, USA

11  
12  
13 \*Corresponding Author: [fadjizaouna.maina@nasa.gov](mailto:fadjizaouna.maina@nasa.gov)

14 **Abstract**

15 In California, it is essential to understand the evolution of water resources in response to a  
16 changing climate to sustain its economy and agriculture and to build resilient communities.  
17 Although extreme conditions have characterized the historical hydroclimate of California, climate  
18 change will likely intensify hydroclimatic extremes by the End of Century (EoC). However, few  
19 studies have investigated the impacts of EoC extremes on watershed hydrology. We use cutting-  
20 edge global climate and integrated hydrologic models to simulate EoC extremes and their effects  
21 on the water-energy balance. We assess the impacts of projected driest, median, and wettest water  
22 years under a Representative Concentration Pathway (RCP) 8.5 on the hydrodynamics of the  
23 Cosumnes river basin. Substantial changes to annual average temperature ( $>+2.5^{\circ}\text{C}$ ) and  
24 precipitation ( $>+38\%$ ) will characterize the EoC extreme water years compared to their historical  
25 counterparts. A shift in the dominant form of precipitation, mostly in the form of rain, is projected  
26 to fall earlier. These changes reduce snowpack by more than 90%, increase peak surface water and  
27 groundwater storages up to 75% and 23%, respectively, and drive the timing of peak storage to  
28 occur earlier in the year. Because EoC temperatures and soil moisture are high, both potential and  
29 actual evapotranspiration (*ET*) increase. The latter, along with the lack of snowmelt in the warm  
30 EoC, cause surface water and groundwater storages to significantly decrease in summer, with  
31 groundwater showing the highest rates of decrease. These changes result in more ephemeral EoC  
32 streams with more focused flow and increased storage in the mainstem of the river network during  
33 the summer.

34 **Keywords:** future climate extremes, integrated hydrologic model, global climate model, end of  
35 century hydrology, watershed hydrology, water management

36           **Introduction**

37           California, the fifth\*largest economy in the world, hosts one of the largest agricultural  
38 regions in the United States and is home to over 39 million people. Because of its geographic  
39 location, Mediterranean climate, geology, and landscape, the state of California is sensitive to  
40 climate change (Hayhoe et al. 2004). Understanding how water resources will evolve under a  
41 changing climate is crucial for sustaining the state’s economy and agricultural productivity. The  
42 region is especially susceptible to climate change given its reliance on the Sierra Nevada Mountain  
43 snowpack as a source of water supply (e.g., Dettinger & Anderson, 2015). Studies show that  
44 temperatures may warm by as much as 4.5°C by the End of Century (hereafter, EoC) (Cayan et  
45 al., 2008), that snowpack is expected to decrease as most precipitation will fall as rain instead of  
46 snow (Siirila-Woodburn, et al., 2021), and that rain on snow events will exacerbate melt (Cayan  
47 et al., 2008; Gleick, 1987; Maurer, 2007; Mote et al., 2005; Musselman, Clark, et al., 2017;  
48 Musselman, Molotch, et al., 2017; Rhoades, Ullrich, & Zarzycki, 2018a). Given that precipitation  
49 falls predominantly in winter months and the summers are hot and dry, the snow accumulated  
50 during the winter provides important water storage for the dry season and is crucial to meet urban  
51 demand, sustain ecosystem function, and maintain agricultural productivity (Bales et al., 2006;  
52 Dierauer et al., 2018). As such, any significant reduction in the snowpack has the potential to  
53 drastically affect the hydrology of the state (Barnett et al., 2005; Harpold & Molotch, 2015; Milly  
54 et al., 2005; Rhoades et al., 2018 a,b).

55           Over the past several decades, researchers have worked to understand how changes in  
56 Sierra Nevada snowpack will affect important hydrologic fluxes such as evapotranspiration (Tague  
57 & Peng, 2013) and streamflow (Berghuijs et al., 2014; Gleick, 1987; He et al., 2019; Maurer, 2007;  
58 Safeeq et al., 2014; Son & Tague, 2019; Vicuna & Dracup, 2007; Vicuna et al., 2007). For

59 example, analyses of recent historical trends show that reductions in snowpack result in increases  
60 in winter streamflow and decreases in the summer streamflow (e.g. Safeeq et al., 2012). However,  
61 the sensitivity of a given area to these climatic changes depends on many factors including geology  
62 and therefore drainage efficiency, topography, and land cover (Alo & Wang, 2008; Christensen et  
63 al., 2008; Cristea et al., 2014; Ficklin et al., 2013; Mayer & Naman, 2011; Safeeq et al., 2015; Son  
64 & Tague, 2019; Tang et al., 2019).

65 Climate change in California is also expected to lead to unprecedented extreme conditions,  
66 which include both severe drought and intense deluge (Swain et al., 2018). In recent years, these  
67 changes have already been observed in the forms of multi-year droughts (Cook et al., 2004; Griffin  
68 & Anchukaitis, 2014; Shukla et al., 2015) and high-intensity precipitation events mainly caused  
69 by atmospheric rivers (Dettinger et al., 2004; Dettinger, 2011; Dettinger, 2013; Ralph & Dettinger,  
70 2011; Ralph et al., 2006). Periods without regular precipitation will require water management  
71 strategies to adapt to ensure demands are met. Similarly, risk management plans and/or  
72 infrastructure for floods, landslides, and other water surplus associated hazards (such as dam  
73 failure) may also require reconsideration. This will be especially true if periods of precipitation,  
74 including those associated with atmospheric rivers, become more extreme, variable, and occur  
75 over a shorter window of time (Swain et al., 2018; Gershunov et al., 2019; Huang et al., 2020;  
76 Rhoades et al., 2020b; Rhoades et al., 2021). Changes in water availability due to climate  
77 “whiplash” will also have important ramifications for water resource management (Wang et al.,  
78 2017; Swain et al., 2018) and significantly increase annual flood damages based on the level of  
79 global warming that occurs (Rhoades et al., 2021). For example, in just the last two decades,  
80 California has experienced the most severe drought in the last 1200 years (Griffin & Anchukaitis,  
81 2014) followed by the wettest year on record (Di Liberto, 2017; SCRIPPS, 2017). These changes

82 in meteorological patterns may become the “new normal”, raising several outstanding questions  
83 related to how these changes in climate will impact the integrated hydrologic cycle, and  
84 subsequently water resource availability for humans and ecosystems.

85 To project how changes in climate will impact watershed behavior, high-resolution,  
86 physics-based models are one of the most promising ways to simulate system dynamics accurately,  
87 particularly those that are non-linear, and constitute a better way to analyze a no-analog future than  
88 the models used in the previous works. Previous studies analyzed future hydrologic conditions in  
89 California but relied on models that do not 1) account for the interactions, feedbacks, and  
90 movements of water from the lower atmosphere to the subsurface; 2) represent groundwater  
91 dynamics and lateral flow; 3) incorporate physics-based high-resolution climate models and/or 4)  
92 hydrologic models (e.g., Berghuijs et al., (2014); Gleick, (1987); He et al., (2019); Maurer, (2007);  
93 Safeeq et al., (2014); Son & Tague, (2019); Vicuna & Dracup, (2007); Vicuna et al., (2007)).  
94 Considerations of coupled interactions that explicitly account for groundwater connections are  
95 important (Condon et al., 2020, 2013; Maxwell and Condon, 2016), especially given groundwater  
96 is the largest reservoir in the terrestrial hydrologic budget and integral to water resource  
97 availability. Also, previous studies have focused on the mid-century period (e.g. Maurer & Duffy,  
98 2005; Son & Tague, 2019), which may indicate a more muted signal in hydrologic impacts than at  
99 EoC. Understanding these impacts is essential because long-term climate projections show that  
100 extremes will be more frequent and significant by the EoC (Cayan et al., 2008).

101 In this work, we assess the impacts of EoC extremely dry and intensely wet conditions on  
102 the hydrodynamics of a Californian watershed that contains one of the last naturally flowing rivers  
103 in the state. This allows us to investigate the impacts of climate change without the complexity of  
104 active water management, and thus to set the context for water management decisions. We

105 specifically investigate how the water and energy balance respond to climate extremes under  
106 climate change, and how those changes propagate to alter the spatiotemporal distribution of water  
107 in different hydrologic compartments of the watershed. We focus our investigation on the changes  
108 in groundwater and surface water storages. The balance of these two natural reservoirs, and their  
109 relationship in response to changes in snowpack reservoir changes, is important for water  
110 management decision making. We aim to 1) strengthen our physics-based understanding of the  
111 main hydrologic processes controlling changes in water storages under a changing climate, 2)  
112 quantify the magnitude and timing of these shifts in storage, and 3) identify the areas that are most  
113 vulnerable to change.

114 To do so, we utilize a novel combination of cutting-edge climate and hydrologic model  
115 simulations. We use an integrated hydrologic model (ParFlow-CLM; Maxwell & Miller, 2005),  
116 which solves the water-energy balance across the Earth's critical zone. When projecting  
117 hydrologic flows, ParFlow-CLM's explicit inclusion of three-dimensional groundwater flow is  
118 important given its demonstrated role in impacting land surface processes like evapotranspiration  
119 (Maxwell & Condon, 2016). We drive Parflow-CLM with climate forcing from a physics-based,  
120 variable-resolution enabled global climate model (the Variable Resolution enabled Community  
121 Earth System Model, VR-CESM; Zarzycki et al., 2014) that dynamically couples multi-scale  
122 interactions within the atmosphere-ocean-land system. This novel pairing of models allows for  
123 several key considerations not present in other methods. Our approach represents both dynamical  
124 and thermodynamic atmospheric response to climate change across scales, different from "pseudo-  
125 global warming" and "statistical delta" approaches used in many hydrologic modeling studies  
126 (e.g., Foster et al., 2020; Rasmussen et al., 2011). While these approaches are useful to isolate the  
127 impact of a given perturbation and/or variable, expected changes in climate will involve the co-

128 evolution of many processes, and may therefore not account for compensating factors. The  
129 interaction between dynamical and thermodynamic responses has important, and sometimes,  
130 offsetting effects on features such as atmospheric rivers. For example, Payne et al. (2020) show  
131 that the thermodynamic response to climate change enhances atmospheric river characteristics  
132 (e.g., Clausius-Clapeyron relationship), whereas the dynamical response diminishes atmospheric  
133 river characteristics (e.g., changes in the jet stream and storm track landfall location). Therefore,  
134 VR-CESM may simulate a more inclusive hydroclimatic response to climate change in the western  
135 United States at a resolution that is at the cutting-edge of today's global climate modeling  
136 capabilities for decadal-to-centennial length simulations (Haarsma et al., 2016).

137         We perform these couplings on spatial and temporal scales relevant for atmosphere-to-  
138 land, and land-to-subsurface interactions, an important consideration, given the recent work  
139 showing the importance of meteorological forcing resolution in representing the hydrologic cycle  
140 (Kampanhout et al., 2019; Maina et al., 2020b; Rhoades et al., 2016; Rhoades, Ullrich, Zarzycki,  
141 et al., 2018c; Wu et al., 2017). Climate conditions for EoC (2070-2100) and a 30-year historical  
142 period (1985-2015) are simulated to identify the median, wettest, and driest water year (WY) in  
143 each. We then simulate the subsequent watershed hydrology of each year using ParFlow-CLM  
144 forced with those meteorological conditions.

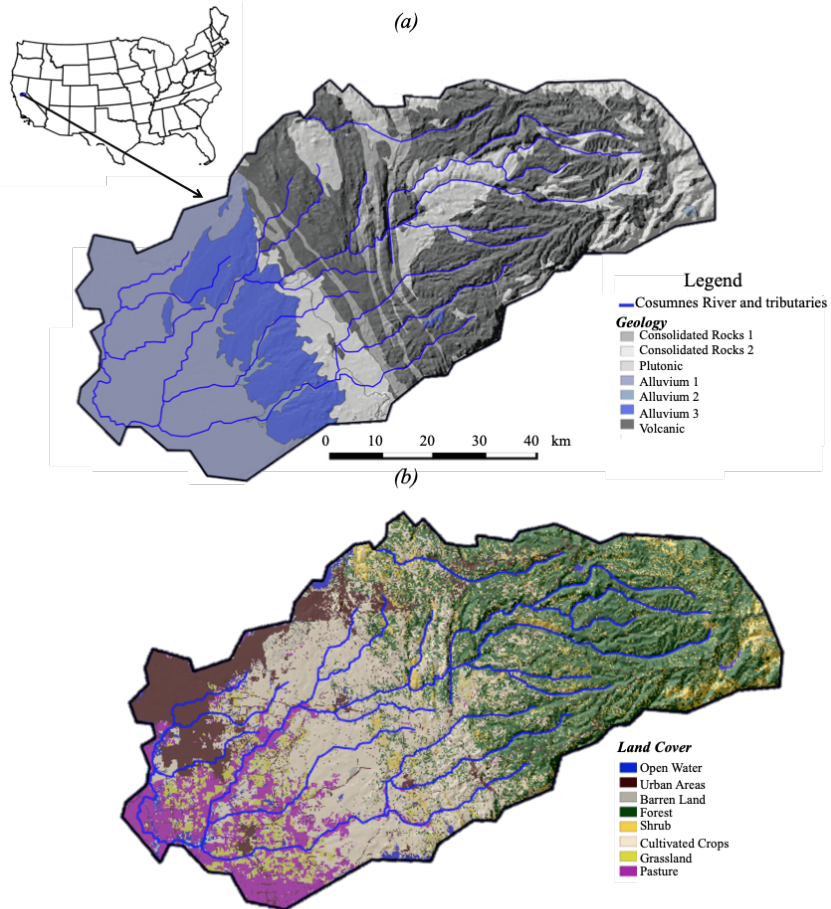
145

## 146         **1. The Cosumnes watershed**

147         The Cosumnes River is one of the last rivers in the western United States without a major  
148 dam, offering a rare opportunity to isolate the impacts of a changing climate on the hydrodynamics  
149 without reservoir management consideration (Maina et al., 2020a; Maina and Siirila-Woodburn,  
150 2020). The watershed spans the Central Valley-Sierra Nevada interface and therefore represents

151 important aspects of the large-scale hydrology patterns of the state, namely the assessment of  
152 interactions between changes in precipitation, snowpack, streamflow, and groundwater across  
153 elevation and geologic gradients. Located in Northern California, USA, the Cosumnes watershed  
154 is approximately 7,000 km<sup>2</sup> in size (Figure 1) and is between the American and the Mokelumne  
155 rivers. Its geology ranges from low-permeability rocks typical of the Sierra Nevada landscape  
156 (volcanic and plutonic) to the porous and permeable alluvial depositions of the Central Valley  
157 aquifers. These are separated by very low-permeability marine sediments. The watershed  
158 topography includes a range of landscapes typical of the region (e.g. varying from flat agricultural  
159 land, rolling foothills, and steep mountainous hillsides), and elevation varies from approximately  
160 2500 m in the upper watershed to sea level in the Central Valley (Figure 1). The Sierra Nevada  
161 mountains are characterized by evergreen forest while the Central Valley hosts an intensive  
162 agricultural region including crops such as alfalfa, vineyards, as well as pastureland. Like other  
163 Californian watersheds, the climate in the Cosumnes is Mediterranean consisting of wet and cold  
164 winters (with a watershed average temperature equal to 0°C) and hot and dry summers (with  
165 watershed average temperature reaching 25°C) (Cosgrove et al., 2003).





166

167 Figure 1: The Cosumnes Watershed (a) location and geology (Jennings et al., 1977), the alluvium  
 168 in blue corresponds to the Central Valley aquifers whereas the consolidated rocks in gray  
 169 correspond to the Sierra Nevada and cross-cutting marine sediments, and (b) land cover (Homer  
 170 et al., 2015).

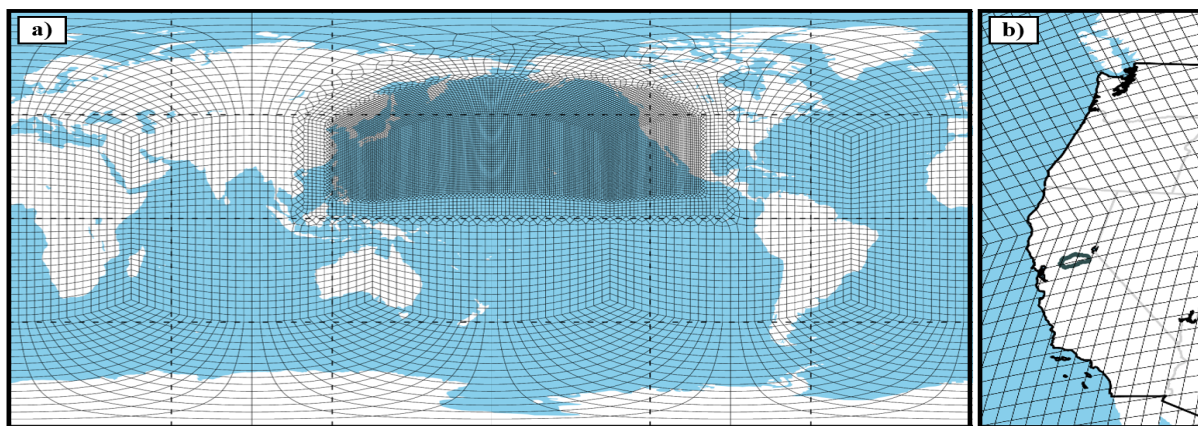
171

## 172 2. Experimental Design

### 173 2.1. Variable Resolution Community Earth System Model (VR-CESM)

174 Historical and EoC meteorological forcings are obtained from a simulation using the VR-  
 175 CESM at a regionally refined resolution of 28 km over the Northern Pacific Ocean through the  
 176 western United States, including the Cosumnes watershed and a global resolution of 111 km

177 (Figure 2). CESM has been jointly developed by NCAR (National Center for Atmospheric  
178 Research) and the DOE (U.S. Department of Energy) and simulates a continuum of Earth system  
179 processes including the atmosphere, land surface, land ice, ocean, ocean waves, and sea ice and  
180 the interactions between them (Collins et al., 2006; Gent et al., 2011; Hurrell et al., 2013). VR-  
181 CESM is a novel tool to perform dynamical downscaling as it allows for the interactions between  
182 the major components of the global climate system (e.g., atmosphere, cryosphere, land surface,  
183 and ocean) while allowing for regional-scale phenomena to emerge where regional refinement is  
184 applied, all within a single model (Huang et al., 2016; Rhoades et al., 2016; Rhoades, Ullrich, &  
185 Zarzycki, 2018b; Rhoades, Ullrich, Zarzycki, et al., 2018c).



186  
187 Figure 2: Variable Resolution Community Earth System Model (VR CESM) grid for (a) globe and  
188 (b) coastal western US with the Cosumnes watershed overlaid in dark gray.

189  
190 The atmospheric model used for these simulations is the Community Atmosphere Model  
191 (CAM) version 5.4 with the spectral element dynamical core, with an atmospheric dynamics time  
192 step of 75 seconds, an atmospheric physics time step of 450 seconds, a prognostic treatment of  
193 rainfall and snowfall in the microphysics scheme (Gettelman and Morrison, 2015) and run under  
194 Atmosphere Model Intercomparison Project (AMIP) protocols (Gates, 1992). Under the AMIP  
195 protocols, the atmosphere and land-surface components of the Earth system model are coupled

196 and periodically bounded by monthly observed sea-surface temperatures and sea-ice extents.  
197 Although this configuration does not exactly recreate historical water years and events, it is  
198 expected to reasonably simulate the distribution of water year types. Also, it should be noted that  
199 the model only projects future conditions, within the envelope of plausible future conditions of the  
200 RCP8.5 scenario and its assumptions of greenhouse gas emissions, sea-surface temperatures, and  
201 sea ice extents and would not be expected to exactly forecast individual water years. Simulations  
202 with VR-CESM are performed for 30-year periods based on the climates from a historical period  
203 (1985-2015) and an EoC period (2070-2100). EoC simulations, analogous to Rhoades, Ullrich, &  
204 Zarzycki, 2018, are bounded by estimates of future changes in ocean conditions derived from a  
205 fully-coupled bias-corrected CESM simulation (assuming historical ocean simulation biases will  
206 be similar in the future simulation) and forced by greenhouse gases and aerosol concentrations  
207 assumed in the RCP8.5 emissions scenario. Historical VR-CESM outputs have been compared  
208 with reanalyses and future VR-CESM outputs have been analyzed for shifts in  
209 hydrometeorological extremes in further detail in Rhoades et al., 2020 a,b. To couple the outputs  
210 with ParFlow-CLM, we regrid the unstructured 28km VR-CESM data over the Cosumnes  
211 watershed using bilinear interpolation in the Earth System Modeling Framework (Jones, 1999) to  
212 a final resolution of approximately 11 km (i.e., 57 grids over the Cosumnes watershed). Notably,  
213 each of the spectral elements in the VR-CESM grid, shown in Figure 1, has a 4x4 set of Gauss–  
214 Lobatto–Legendre (GLL) quadrature nodes where equations of the atmospheric model are solved  
215 (Herrington et al., 2019). Therefore, the actual resolution at which the atmospheric dynamics and  
216 physics are solved in VR-CESM are at higher-resolution (~28km) than is shown in Figure 1,  
217 making these some of the highest resolution global Earth system model simulations over California  
218 to date (Haarsma et al., 2016).

219 To identify if VR-CESM is fit for purpose to simulate historical dry, median, and wet WYs,  
220 and inform potential biases in future projections (over California and, more specifically, the  
221 Cosumnes watershed), we first conduct a model comparison to a widely used observational  
222 product, the Parameter-elevation Relationships on Independent Slopes Model (PRISM; Daly et al.,  
223 2008) at 4 km resolution analogous to Rhoades et al., (2020a). However, in this study, we focus  
224 our assessment of VR-CESM fidelity over California and the Cosumnes watershed. PRISM  
225 provides daily precipitation, mean dewpoint temperature and maximum and minimum surface  
226 temperature, and vapor pressure. PRISM precipitation and temperature data spanning 1981-2019  
227 are compared with the VR-CESM 1985-2015 simulations. We note that a mismatch in the time  
228 period (1981-2019 versus 1985-2015) is deliberate. As stated previously, VR-CESM is simulated  
229 under AMIP-protocols (bounded by monthly observed sea-surface temperatures and sea-ice  
230 extents), and therefore we do not expect VR-CESM to exactly recreate past historical WYs.  
231 However, we do expect that our 30-year simulation can reasonably recreate the range of WY types  
232 over California and the Cosumnes, which is why we utilize the broader range of PRISM WYs that  
233 are available. For this comparison, we regrid the unstructured VR-CESM data to 4km resolution  
234 (the native resolution of PRISM) using the Earth System Modeling Framework (ESMF) Offline  
235 Re-gridding Weight Generator in the NCAR Command Language (NCL, 2021).

236 The comparison (discussed in appendix A) indicates that VR-CESM reasonably reproduces  
237 the historical WY conditions (i.e., interannual range of PRISM precipitation largely overlaps with  
238 the range of model bias simulated by VR-CESM). VR-CESM generally simulates a wetter  
239 historical period over the Cosumnes (range of bias of 1330 mm) relative to PRISM (range of  
240 interannual variability of 1320 mm). Basin-average minimum (421 mm) and maximum (1740 mm)  
241 WY accumulated precipitation are slightly larger than those of PRISM. Of relevance to this study,

242 PRISM has shown notable uncertainties in the Sierra Nevada. Lundquist et al., 2015 showed that  
 243 an underrepresentation of the most extreme storm total precipitation in the Sierra Nevada can result  
 244 in an upper-bound uncertainty of 20% in WY accumulated precipitation in PRISM. Therefore, the  
 245 wettest WY simulated by VR-CESM is well within the 20% uncertainty range of PRISM's wettest  
 246 WY ( $1580 \pm 316$  mm). Further, differences in basin-average WY accumulated precipitation  
 247 between VR-CESM and PRISM are non-significant using a t-test and assuming a p-value  $< 0.05$ .  
 248 As discussed in further detail below, we posit that atmospheric river-related precipitation is likely  
 249 the driver of the wet bias mismatch with PRISM. However, we also note that the uncertainty  
 250 bounds of the PRISM product WY precipitation totals in the Sierra Nevada are estimated to be  
 251 upwards of  $\sim 20\%$  too dry (e.g., Lundquist et al., 2015), particularly for extreme precipitation  
 252 events such as atmospheric rivers and in mountainous terrain.

253

## 254 **2.2. Integrated Hydrologic Model: ParFlow-CLM**

255 The integrated hydrologic model ParFlow-CLM (Kollet & Maxwell, 2006; Maxwell, 2013;  
 256 Maxwell & Miller, 2005) solves the transfer and interactions of water and energy from the  
 257 subsurface to the lower atmosphere including groundwater dynamics, streamflow, infiltration,  
 258 recharge, evapotranspiration, and snow dynamics. The model describes 3D groundwater flow in  
 259 variably saturated media with the Richards equation (equation 1, Richards, 1931) and 2D overland  
 260 flow with the kinematic wave equation (equation 2).

$$261 \quad S_S S_W(\psi_P) \frac{\partial \psi_P}{\partial t} + \phi \frac{\partial S_W(\psi_P)}{\partial t} = \nabla \cdot [K(x) k_r(\psi_P) \nabla(\psi_P - z)] + q_s \quad (1)$$

262 Where  $S_S$  is the specific storage ( $L^{-1}$ ),  $S_W(\psi_P)$  is the degree of saturation (-) associated  
 263 with the subsurface pressure head  $\psi_P$  (L),  $t$  is the time (T),  $\phi$  is the porosity (-),  $k_r$  is the relative

264 permeability (-),  $z$  is the depth,  $q_s$  is the source/sink term ( $T^{-1}$ ) and  $K(x)$  is the saturated hydraulic  
265 conductivity ( $L T^{-1}$ ).

266 ParFlow solves the mixed form of the Richards equation which has the advantage of  
267 conserving the mass (Celia et al., 1990).

268 The kinematic wave equation is used to describe surface flow in two dimensions is defined  
269 as:

$$270 \quad -k(x)k_r(\psi_0)\nabla(\psi_0 - z) = \frac{\partial\|\psi_0,0\|}{\partial t} - \nabla \cdot \vec{v}\|\psi_0,0\| - q_r(x) \quad (2)$$

271 Where  $\psi_0$  is the ponding depth,  $\|\psi_0,0\|$  indicates the greater term between  $\psi_0$  and 0,  $\vec{v}$  is  
272 the depth averaged velocity vector of surface runoff ( $L T^{-1}$ ),  $q_r$  is a source/sink term representing  
273 rainfall and evaporative fluxes ( $L T^{-1}$ ).

274 Surface water velocity at the surface in  $x$  and  $y$  directions, ( $v_x$ ) and ( $v_y$ ) respectively, is  
275 computed using the following set of equations:

$$276 \quad v_x = \frac{\sqrt{S_{f,x}}}{m} \psi_0^{\frac{2}{3}} \text{ and } v_y = \frac{\sqrt{S_{f,y}}}{m} \psi_0^{\frac{2}{3}} \quad (3)$$

277 Where  $S_{f,x}$  and  $S_{f,y}$  friction slopes along  $x$  and  $y$  respectively and  $m$  is the manning coefficient.

278 ParFlow employs a cell-centered finite difference scheme along with an implicit backward Euler  
279 scheme and the Newton Krylow linearization method to solve these nonlinear equations. The  
280 computational grid follows the terrain to mimic the slope of the domain (Maxwell, 2013).

281 ParFlow has many advantages in comparisons to other hydrologic models. Compared to  
282 other hydrologic models (MODFLOW (Harbaugh, 2005), FEFLOW (Trefry and Muffels, 2007),  
283 SWAT (Soil and Water Assessment Tool) (Neitsch et al., 2000), SAC-MA (Sacramento Soil  
284 Moisture Accounting Model)), ParFlow has the advantages of accounting for land surface  
285 processes such as snow dynamics and evapotranspiration and their interactions with the subsurface  
286 which are crucial for studying the hydrology of California. ParFlow also solved the subsurface

287 flow by accounting for variably saturated conditions, an important feature for calculating  
288 groundwater recharge and the connection between the groundwater and the land surface processes,  
289 which is not the case for the aforementioned models. While some hydrologic models have a better  
290 representation of the land surface processes (Noah-MP (Niu et al., 2011), VIC (Variable  
291 Infiltration Capacity Model Macroscale Hydrologic Model) (Liang et al., 1994)), these models do  
292 not have a detailed representation of the subsurface flows. Because the surface flow is important  
293 in the region and it establishes the connection between the headwaters and the valleys, its good  
294 representation is essential for projecting changes in hydrology. Compared to other integrated  
295 hydrologic models (CATHY (Catchment Hydrology) (Bixio et al., 2002), MIKE-SHE (Abbott et  
296 al., 1986)), ParFlow has the advantages of solving a two-dimensional kinematic flow equation that  
297 is fully coupled to the Richards equation.

298 ParFlow is coupled to the Community Land Model (CLM) to solve the surface energy and  
299 water balance, which enables interactions between the land surface and the lower atmosphere and  
300 the calculation of key land surface processes governing the system hydrodynamics such as  
301 evapotranspiration, infiltration, and snow dynamics. CLM models the thermal processes by closing  
302 the energy balance at the land surface given by:

$$303 \quad R_n(\theta) = LE(\theta) + H(\theta) + G(\theta) \quad (4)$$

304 Where  $\theta = \phi S_w$  is the soil moisture,  $R_n$  is the net radiation at the land surface (E/LT) a  
305 balance between the shortwave (also called solar) and longwave radiation,  $LE$  is the latent heat  
306 flux (E/LT) which captures the energy required to change the phase of water to or from vapor,  $H$   
307 is the sensible heat flux (E/LT) and  $G$  is the ground heat flux (E/LT).

308 More information about the coupling between ParFlow and CLM can be found in Maxwell  
309 & Miller, (2005). CLM uses the following outputs of the VR-CESM model at 3-hourly resolution

310 to solve the energy balance at the land surface: precipitation, air temperature, specific humidity,  
311 atmospheric pressure, north/south and east/west wind speed, and shortwave and longwave wave  
312 radiation.

313 We constructed a high-resolution model of the Cosumnes watershed with a horizontal  
314 discretization of 200 m and vertical discretization that varies from 10 cm at the land surface to 30  
315 m at the bottom of the domain. The model has 8 layers, the first 4 layers represent the soil layers  
316 and the other four the deeper subsurface. The total thickness of the domain is 80 m to ensure  
317 appropriate representation of water table dynamics. Observed water table depths (as measured at  
318 several wells located in the Central Valley portion of the domain) vary between approximately 50  
319 m and the land surface through a multi-year time period (Maina et al., 2020a). Therefore, to be  
320 conservative for imposing the lower boundary layer, anything below 80 m is expected to remain  
321 fully saturated. The resulting model comprises approximately 1.4 million active cells and was  
322 solved using 320 cores in a high-performance computing environment. The Cosumnes watershed  
323 is bounded by the American and Mokelumne rivers. We, therefore, impose weekly varying values  
324 of Dirichlet boundary conditions along these borders to reflect the observed changes of river  
325 stages. The eastern part of the watershed corresponding to the upper limit in the Sierra Nevada is  
326 modeled as a no-flow (i.e., Neumann) boundary condition. Hydrodynamic parameters required to  
327 solve the surface and subsurface flows (e.g., hydraulic conductivity, specific storage, porosity, and  
328 van Genuchten parameters) are derived from a regional geological map (Geologic Map of  
329 California, 2015; Jennings et al., 1977) and a literature review of previous studies (Faunt et al.,  
330 2010; Faunt and Geological Survey (U.S.), 2009; Gilbert and Maxwell, 2017; Welch and Allen,  
331 2014). We use the 2011 National Land Cover Database (NLCD) map (Homer et al., 2015) to  
332 define land use and land cover required by CLM. We further delineate specific croplands (notably



333 alfalfa, vineyards, and pasture) in the Central Valley by using the agricultural maps provided by  
334 the National Agricultural Statistics Service (NASS) of the US Department of  
335 Agriculture's (USDA) Cropland Data Layer (CDL) (Boryan et al., 2011). Vegetation parameters  
336 are defined by the International Geosphere-Biosphere Programme (IGBP) database (IGBP, 2018).  
337 A complete description of the model parameterization can be found in appendix B and more details  
338 in Maina et al. (2020a). The model has been extensively calibrated and validated using various  
339 datasets, including remotely sensed data and ground measurements, which are however very sparse  
340 in the area. Model validation which consists in comparing both surface and subsurface  
341 hydrodynamics (groundwater and river stages) and land surface processes was performed over a  
342 period of three years that includes extremely dry and wet water years (Appendix C). We  
343 specifically compared simulated and measured river stages at three stations located in the Sierra  
344 Nevada headwater, foothill, and the Central Valley. The annual averages absolute differences  
345 between measurements and simulations were between 0.4 and 0.8 m. We selected four wells in the  
346 Cosumnes watershed based on their availability of data to compare measured and simulated  
347 groundwater levels. These wells are sparsely distributed in the Central Valley. The absolute  
348 differences between observed and simulated groundwater levels vary between 0.47 to 3.73 m. The  
349 highest absolute differences were attributed to the lack of best estimations of groundwater pumping  
350 rates in the region. Nonetheless, the reasonable agreement between observations and simulated  
351 variables over a period that includes both extremely dry and intensely wet conditions has allowed  
352 us to conclude that the model can capture these extreme dynamics. We rely on remote sensing  
353 data to assess the ability of our model to simulate key land surface processes (evapotranspiration  
354 *ET*, soil moisture, and snow water equivalent *SWE*). We compared the simulated *SWE* to SNODAS  
355 (The National Weather Service's Snow Data Assimilation, National Operational Hydrologic

356 Remote Sensing Center, 2004) and a *SWE* reanalysis by Bair et al., (2016). Our comparisons  
357 indicated that the absolute differences between our *SWE* values and these data were equal to 3 mm  
358 on average. Moreover, the simulated key parameters controlling the snow dynamics such as peak  
359 snow and timing of snow ablation were also in agreement with remotely sensed data for both dry  
360 and wet years (Appendix C). Absolute differences between the simulated *ET* and the remotely  
361 sensed *ET* from METRIC (Mapping Evapotranspiration at High Resolution with Internalized  
362 Calibration, Allen et al., 2007) were equal to 0.036 mm/s while the differences between the  
363 simulated soil moisture and the SMAP (Soil Moisture Active Passive, SMAP, 2015) soil moisture  
364 were 0.2. More details about model calibration and validation can be found in Appendix C and  
365 previous publications (Maina et al., 2020a, Maina et al., 2020b; Maina and Siirila-Woodburn,  
366 2020c). The model has also been successfully used in recent investigations of post-wildfire and  
367 climate extremes hydrologic conditions and to assess the role of meteorological forcing scale on  
368 simulated watershed dynamics (Maina et al., 2020a, b; Maina and Siirila-Woodburn, 2020c).  
369 Initial conditions for pressure-head were obtained by a spin-up procedure using the forcing of the  
370 historical median WY. We recursively simulated the historical median WY forcing until the  
371 differences of storage at the end of the WY were less than 1%, indicating convergence. This  
372 pressure head field is then used as the initial condition for each of the five WYs of interest (i.e.,  
373 the EoC wet, EoC dry, historic wet, historic dry, EoC median). Though we acknowledge land  
374 cover alterations are expected to occur by the EoC (either naturally or anthropogenically), in this  
375 work we assume that the vegetation remains constant for both historical and EoC simulations for  
376 simplicity. Although outside of the scope of this work, future studies will investigate the impacts  
377 of an evolved land use/land cover, vegetation physiology, and resilience strategies to manage water  
378 resources. Further, while the Central Valley of California hosts intensive agriculture that is reliant

379 on groundwater pumping for irrigation, we didn't incorporate pumping and irrigation in our model  
 380 configuration. We did this with the assumption that groundwater pumping rates may substantially  
 381 change in the future due to new demands, policies, regulations, and changes in land cover and land  
 382 use and aim to provide an estimate of the natural hydrologic system response to climate change.

383

### 384 **2.3. Analysis of EoC hydrodynamics**

385 To investigate how the EoC climate extremes affect water storages, we investigate five  
 386 hydrologic variables: *SWE*, *ET*, Pressure-head ( $\psi$ ) distributions, and surface and subsurface water  
 387 storage. Total groundwater (GW) storage is given by:

$$388 \quad Storage_{GW} = \sum_{i=1}^{n_{GW}} \Delta x_i \times \Delta y_i \times \Delta z_i \times \psi_i \times \left( \frac{S_{s_i}}{\phi_i} \right) \quad (5)$$

389 where  $n_{GW}$  is the total number of subsurface saturated cells (-),  $\Delta x_i$  and  $\Delta y_i$  are cell discretizations  
 390 along the x and y directions (L),  $\Delta z_i$  is the discretization along the vertical direction the cell (L),  
 391  $S_{s_i}$  is the specific storage associated with cell  $i$ ,  $\psi_i$  the pressure-head, and  $\phi_i$  is the porosity.

392 Total surface water (SW) storage which accounts for any water located at the land surface  
 393 (i.e., any cell of the model with a pressure-head greater than 0) and includes river water or overland  
 394 flow is calculated via:

$$395 \quad Storage_{SW} = \sum_{i=1}^{n_{SW}} \Delta x_i \times \Delta y_i \times \psi_i \quad (6)$$

396 where  $n_{SW}$  is the total number of cells with surface water i.e., with surface  $\psi$  greater than 0 (-),  
 397 and  $i$  indicates the cell.

398 We compare each EoC WY simulation to its corresponding historical WY counterpart and  
 399 both the historical and EoC medians. This allows us to assess how EoC extremes change relative  
 400 to what is currently considered an extreme condition as well as to “normal” in the relevant time.  
 401 Comparisons are shown as a percent change (*PC*) calculated using:

$$PC_{i,t} = \frac{X_{projection_{i,t}} - X_{baseline_{i,t}}}{X_{baseline_{i,t}}} \times 100 \quad (3)$$

where  $X$  is the model output ( $ET$ ,  $SWE$ , or  $\psi$ ) at a given point in space ( $i$ ) at a time ( $t$ ), *baseline* is the selected simulation (historical median, EoC median, or historical extreme), and *projection* represents the simulation obtained with the EoC extreme WYs (dry or wet).

406

### 407 **3. Results**

408 In this section, we present a subset of the outputs from VR-CESM (precipitation and  
 409 temperature) to identify the extreme (dry and wet) and median WYs of interest. Changes in fluxes  
 410 and storages over the course of each WY, as well as the spatial variability of these changes in two  
 411 important periods of the WY (peak flow and baseflow) are also shown.

412

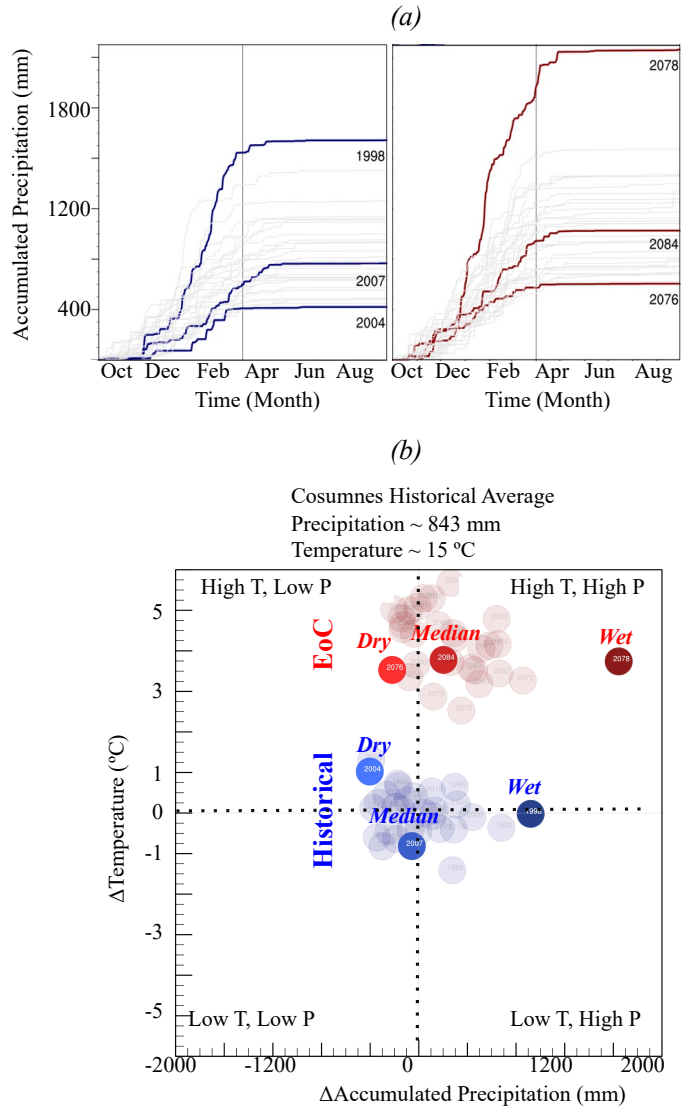
#### 413 **3.1. Selection of the median, dry, and wet WYs**

414 From the historical and EoC 30-year VR-CESM simulations we select the median, wettest,  
 415 and driest WYs for comparison (see Figure 3a). Overall, the future WYs are ~30% wetter than the  
 416 historical WYs (p-value ~0.006 for two-tailed t-test of equal average annual precipitation) in  
 417 addition to being ~4.6°C warmer. Precipitation and temperature variances are mostly similar in the  
 418 historical and EoC simulations, though EoC minimum temperature may be more variable (p-value  
 419 ~0.059 for two-tailed f-test of equal variance in minimum temperature). On average the timing for  
 420 the start, length, and end of precipitation is similar, though EoC precipitation may be less variable  
 421 in its start time (p-value ~0.053 for f-test of equal variance in days to reach 5<sup>th</sup> percentile of annual  
 422 precipitation). In the climate model, there are no clear trends between the precipitation timing  
 423 metrics and total amount of precipitation.

424           The EoC median WY is much wetter than its historical counterpart, with about ~250 mm  
425 more precipitation that begins approximately 1 week earlier and ends approximately 2 weeks  
426 earlier in the year. The EoC wettest WY is much wetter than the historical wettest WY and is  
427 characterized by 42% more precipitation. This is consistent with Allan et al. (2020), who suggest  
428 a wetter future. The EoC wettest WY is 3.8°C warmer than the historical wettest WY and 4.6°C  
429 warmer than the historical median WY, as the historical median WY is one of the coolest years in  
430 the series. Precipitation occurs earlier in the EoC wet WY compared to the historical wet or median  
431 WYs, with the 5<sup>th</sup> percentile of precipitation reached 12 days earlier in the EoC wettest WY than  
432 either the wettest or median historical WYs. The duration of the EoC wettest WY precipitation  
433 season (146 days) is between the historical wettest WY (133 days) and the historical median WY  
434 (155 days).

435           The EoC dry WY is also much wetter than its historic counterpart; in fact, the EoC dry WY  
436 is wetter than the seven driest historical WYs of the 30-year historical ensemble. Simulation of 30  
437 random draws from two identical normal distributions, repeated 100,000 times, finds that the  
438 lowest value in one is higher than the seven lowest values in the other only ~1.1% of the time (p-  
439 value ~0.011). This statistical test reveals that this VR-CESM simulation suggests that future dry  
440 years will be somewhat wetter than historical dry years. The EoC dry WY is only ~2.5°C warmer  
441 than the historical dry WY. The divergence in temperature is smaller for the comparison of EoC  
442 and historical WYs of the dry extremes as opposed to the wet extremes because the historical dry  
443 WY is the second-warmest WY in the historical simulations, while the EoC dry WY is the third  
444 coolest in the EoC simulations. Precipitation in the EoC dry WY starts particularly early, with the  
445 5<sup>th</sup> percentile of annual precipitation reached by mid-October. This is much earlier than either the  
446 dry or median historical WYs, which don't reach that percentile of precipitation until mid-to-late

447 November. The historical dry WY also has a particularly short precipitation duration of only 97  
 448 days, while the EoC dry WY has a 163-day precipitation duration, more similar to the median  
 449 historical WY duration of 155 days.

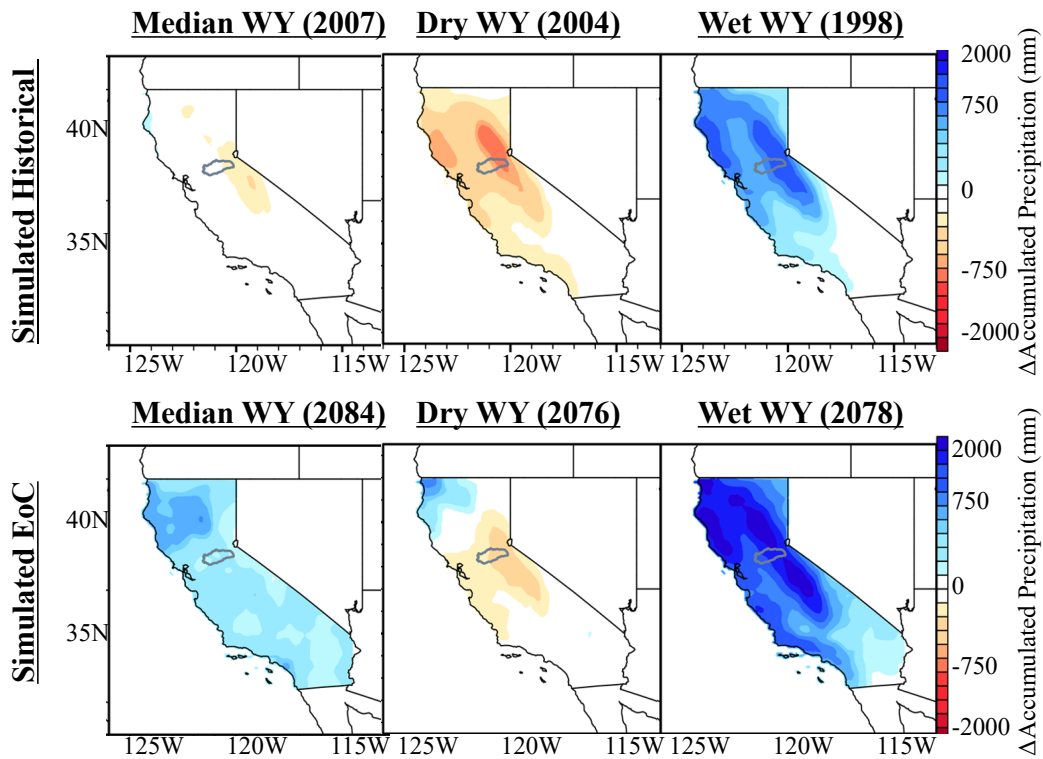


450  
 451 Figure 3: (a) VR-CESM accumulated total precipitation for the historical and End of Century  
 452 (EoC) simulations, and (b) quadrants for differences between each individual water year (WY)  
 453 and the historical average temperature and accumulated precipitation in the Cosumnes watershed.  
 454 The historical and EoC dry, median and wet WYs are indicated in blue and red, respectively.

455

456 Figure 4 shows the spatial distribution of accumulated precipitation anomalies across  
457 California. These anomalies are computed for each of the six identified WYs relative to the  
458 climatological average (the 30-year historical mean). These spatial plots provide context for the  
459 changes modeled in the Cosumnes watershed relative to broader precipitation changes California-  
460 wide. As in the Cosumnes, California-wide EoC dry, median, and wet WYs are all characterized  
461 by higher precipitation totals than their historical counterparts. Importantly, the EoC wet WY is a  
462 true outlier not only in the Cosumnes but across California too. California lies at an important  
463 large-scale circulation transition, namely semi-permanent high-pressure systems associated with  
464 the Hadley circulation. Therefore, how climate change alters the atmospheric dynamics over  
465 California, or more specifically how far northward storm-tracks may shift, remains uncertain and  
466 depends on climate model choice. This has led to papers that claim the future of California will be  
467 wet across a range of climate models (e.g., Neelin et al, 2013; Swain et al., 2013; Gershunov et al.,  
468 2019; Rhoades et al., 2020b; Persad et al., 2020) and, for select climate models, that it could be  
469 drier. Notably, these studies highlight an asymmetric response in the frequency of wet versus dry  
470 WYs (i.e., anomalously wet WYs increase in frequency much more in the future than anomalously  
471 dry WYs). Many of the aforementioned studies also highlight that in anomalously wet WYs  
472 extreme precipitation events (e.g., atmospheric rivers) will occur with greater intensity and  
473 frequency and largely drive changes in WY precipitation totals (which is shown in our VR-CESM  
474 simulations for California in more detail in Rhoades et al., 2020b). Given these complexities and  
475 others such as consideration for how dynamical and thermodynamical effects of climate change  
476 may interact with one another to offset or amplify extreme precipitation events (Payne et al., 2020),  
477 the hypothesis that global warming will result in a climate where the “wet gets wetter and dry gets  
478 drier” may be too simplistic of an assumption for California. Rhoades et al., (2020b) shows

479 quantitatively that the increases in precipitation observed in the VR-CESM outputs are due to a  
 480 greater number of intense atmospheric river events that occur more regularly back-to-back, which  
 481 was recently corroborated by Rhoades et al. (2021) using uniform-high-resolution CESM  
 482 simulations at different warming scenarios, and that atmospheric river precipitation totals increase  
 483 at a much larger rate (+53%/K) than non-AR precipitation totals (+1.4%/K), which agrees with  
 484 findings made in other studies such as Gershunov et al. (2019).



485  
 486 Figure 4: Precipitation spatial distributions of the dry, median, and wet water years (WY) for the  
 487 30-year historical and EoC simulations relative to the climatological average (derived from the 30-  
 488 year historical mean)

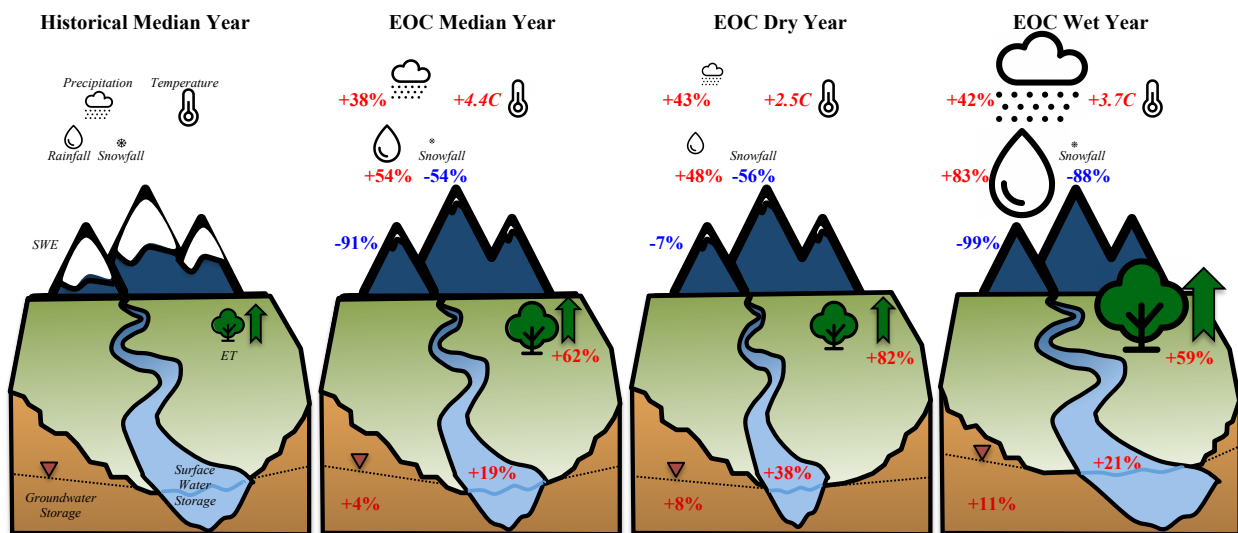
489

### 490 3.2. Changes in annual watershed-integrated fluxes and storages

491 Figure 5 illustrates the annual changes in the integrated hydrologic budget of the Cosumnes  
 492 watershed for the EoC WYs (i.e., median, dry, and wet) compared to the historical median WY.



493 The EoC median WY compared to the historical median WY has 38% more precipitation and the  
 494 temperature is 4.4°C higher. Further, the precipitation phase also shifts with an increase in rainfall  
 495 (54%) and a decrease in snowfall (-54%). This results in a significant decrease in *SWE* (-91%)  
 496 which is consistent with many other studies that have shown that increased temperatures due to  
 497 climate change will lead to low-to-no snow conditions (Berghuijs et al., 2014; Cayan et al., 2008;  
 498 Mote et al., 2005; Rhoades et al., 2018 a,b; Son & Tague, 2019). The increase in temperature and  
 499 precipitation results in an increase in *ET* (62%), consistent with the findings of other recent studies  
 500 (e.g. McEvoy et al., 2020). Nevertheless, the larger amount of precipitation associated with the  
 501 EoC is enough to offset higher *ET* demand and recharge groundwater and surface water, which  
 502 experience an increase of 4% and 19% respectively. The EoC wet WY has similar changes as the  
 503 EoC median WY when compared to the historical wet WY yet the magnitude of the increase in  
 504 surface (21%), and groundwater (11%) storages are higher due to more precipitation and higher  
 505 temperatures. The dry EoC WY is also characterized by higher precipitation (43%, the largest  
 506 increase) than its historical counterpart, this results in large increases in total groundwater (8%)  
 507 and surface water (38%) storages.



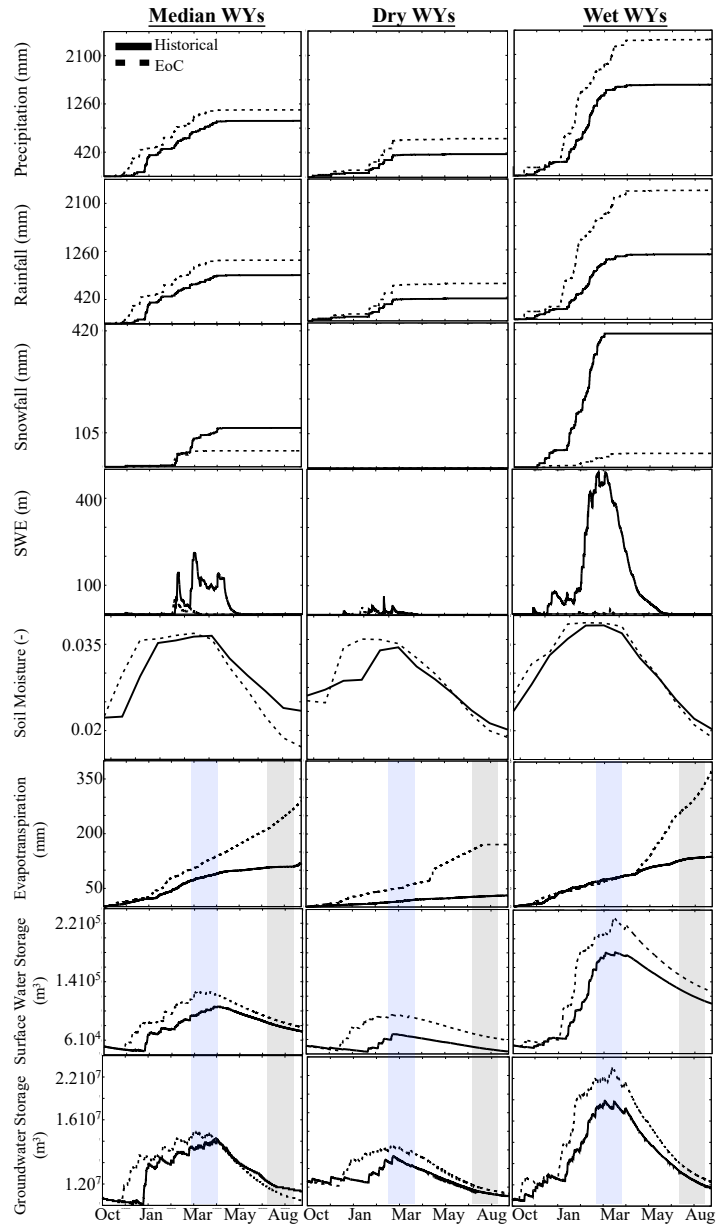
508

509 Figure 5: Annual percent changes in precipitation, rainfall, snowfall, temperature, *SWE*, *ET*,  
510 surface water, and groundwater storages in the EoC water years (WY) (i.e median, dry, and wet)  
511 at the watershed scale relative to their historical counterparts. Info-graphic size scaled to EoC  
512 conditions.

513

### 514 **3.3. Temporal variation of watershed-integrated fluxes and storages**

515 Understanding the annual changes at the watershed scale is important to broadly  
516 understand changes in the water budget in response to future climate extremes. However, a deeper  
517 understanding of the processes that drive these changes and the interactions from atmosphere-  
518 through-bedrock requires an analysis of their spatiotemporal variations as well. Figure 6 shows  
519 the temporal variations of each of the historical and EoC WY's integrated hydrologic budgets  
520 grouped by WY type (columns), with a top-down sequencing of hydrologic variables of interest in  
521 order from the atmosphere through subsurface (rows). This organization allows for the  
522 investigation of propagating impacts to be directly compared in time. In this section, we discuss  
523 historical vs EoC changes observed in each of the WY types (i.e., median, dry, and wet). Each WY  
524 shows unique hydrodynamic behaviors and changes compared to the historical conditions. The  
525 median WY sheds light on how changes in the precipitation phase and increases in temperature  
526 and precipitation in the EoC will impact the hydrodynamics. The dry WYs allow comparing EoC  
527 and historical low-to-no snow conditions whereas assessing the hydrodynamics of the EoC wet  
528 WY provides a better understanding of how intense EoC precipitation along with the warm EoC  
529 climate will shape the hydrology.



530

531 Figure 6: Temporal variations of the total cumulative precipitation, rainfall, and snowfall at the  
 532 watershed scale, total *SWE* at the watershed scale, the average watershed values of soil moisture,  
 533 the cumulative watershed *ET*, and the total surface water, and groundwater storages at the  
 534 watershed scale associated with the six historical and EoC Water Years (WY). The blue area  
 535 indicates the selected peak flow period while the gray area corresponds to the selected baseflow  
 536 conditions for the spatial distribution analyses.

537

538

### 3.3.1. Median water years

539

540

541

542

543

544

545

546

547

548

As indicated in section 3.1, the EoC median WY has more precipitation than the historical median WY. The EoC precipitation comes mainly as rain due to the warmer temperatures of the EoC and includes virtually no snowfall from late winter to early spring. This precipitation phase-change combined with the earlier snowfall cessation date in the WY results in minimal and even non-existent *SWE* in the Cosumnes watershed for much of the WY, a significant change compared to historic conditions. EoC peak *SWE* occurs in February in contrast to the historical peak *SWE*, which occurs in April. Due to the watershed's relatively low elevation, snow accumulates only in the upper part of the Cosumnes watershed (~10% of the total watershed area). Only areas located in the highest elevations (> 2000 m), such as the eastern limit of the watershed, show any *SWE* in the EoC simulations whereas in the historical WYs we observed *SWE* as low as 1000 m.

549

550

551

552

553

554

The decrease in snow and the increase in rain along with an earlier onset of seasonal precipitation directly impacts soil moisture, which sees an early increase with a slightly higher peak than historical. As more water is available earlier in the EoC, the *ET* demand from increased temperatures is met until substantially higher summer temperatures increase *ET* at a much faster rate than the historical WY. The high EoC *ET* and the lack of snowmelt cause the soil to rapidly dry from late-spring through late-summer.

555

556

557

558

559

Because of the marked increase in total precipitation and shift from snow to rain in the EoC simulations, surface water storage generally increases throughout the WY. This is consistent with previous studies (Gleick, 1987; He et al., 2019; Maurer, 2007; Safeeq et al., 2014; Son & Tague, 2019; Vicuna & Dracup, 2007; Vicuna et al., 2007). Surface water storage increases in early November in the EoC simulations while in the historical simulations this increase occurs in

560 January. Similar to the earlier peak *SWE* and soil moisture, the peak surface water storage in the  
561 EoC is also earlier (January through February) compared to the historical period (March through  
562 April). This late-season surface water storage remains larger because the accumulated precipitation  
563 is large enough to overcome the increased *ET* in a warmer climate. Similar to surface water storage,  
564 groundwater storage increases earlier and peaks at a larger amount than the historical WY.  
565 However, in contrast to the surface water storage, the groundwater storage during baseflow  
566 conditions is lower in the median EoC compared to the median historical year. This decrease in  
567 groundwater during baseflow conditions is due to the lack of snowmelt and higher EoC *ET*. In late  
568 spring and summer in the EoC, groundwater keeps depleting through *ET* and is not recharged by  
569 snowmelt through surface and subsurface flows from the Sierra Nevada as in the historical period.  
570 This may indicate that compared to surface water storages, groundwater storage may be more  
571 sensitive to EoC hydroclimatic changes (which are multi-fold, and in this case include an increase  
572 in precipitation, a transition from snow to rain, and higher *ET*). One way to quantitatively measure  
573 this sensitivity is to compare the seasonal change in water storage between peak and baseflow  
574 conditions. Historically, changes between peak and baseflow conditions (i.e., the amount of water  
575 lost between peak and base flow) resulted in moderate seasonal changes in groundwater storage  
576 (30%) and surface water storage (32%). The EoC simulations reveal larger seasonal variation for  
577 groundwater and surface water storage (40% and 37% decreases, respectively). Groundwater in  
578 the Cosumnes Watershed is mainly recharged in the headwaters and stored in the Central Valley.  
579 Therefore, these Central Valley aquifers experience earlier and larger increases in storage which  
580 lead to more water available to *ET* and therefore aquifer depletion. A deeper understanding of this  
581 phenomenon requires an analysis of the spatial patterns of these changes which is performed later  
582 on in this study.

583  
584  
585  
586  
587  
588  
589  
590  
591  
592  
593  
594  
595  
596  
597  
598  
599  
600  
601  
602  
603  
604  
605

### 3.3.2. Dry water years

All EoC WYs are characterized by higher precipitation in the form of rainfall compared to their historical counterparts. The historical dry WY has ~43% less total precipitation than the EoC dry WY. However, we note that for the EoC dry WY the decrease in snowfall is less drastic than the median or wet EoC years. This is because the historically driest WY is significantly warmer than the historical average WY, and therefore already has a smaller snowpack, 94% lower than the historical median WY. The EoC dry WY *SWE* also accumulates two months earlier than the historical *SWE*. Because the differences in *SWE* between the dry WYs are smaller than the differences in *SWE* between the median WYs (7% versus 91%), we can deduce that the early and larger rise in soil moisture in the EoC dry WY is mostly due to an earlier and larger amount of rainfall. The higher soil moisture and EoC temperatures result in higher *ET* throughout the WY compared to the historical WY. This *ET* results in lower soil moisture by the end of the summer, similar to the median WY. In addition, surface water storage peaks earlier and at a larger amount compared to the historical WY. The surface water storage in the EoC remains higher throughout the WY compared to its historical counterpart despite this higher *ET* due to the low precipitation associated with the historical dry WY. We further note that the difference in surface water storage during baseflow conditions between the two dry WYs is higher than the difference between the two median WYs. The groundwater recharge starts two months earlier in the EoC driest WY compared to the historical driest WY due to the changes in timing and magnitude of precipitation. However, it is interesting to note that groundwater storage during baseflow conditions in the EoC WY is nearly equal to the historical WY (within 3%). Thus, although more water enters the EoC dry WY system through greater precipitation, it eventually exits by the end of the WY and no

606 considerable net gains to groundwater are observed. This significant reduction in groundwater  
607 storage from late winter to end-of-summer is a result of the much larger EoC *ET* and highlights  
608 the dynamic nature of the EoC dry year watershed interactions. Also similar to the median WY,  
609 dry WY seasonal decreases in EoC storage are more pronounced in the groundwater signal (36%)  
610 than in the surface water signal (33%). We further note that the decreases in groundwater and  
611 surface water storages are, as in the median WY, larger (+8%) than the historical decreases.

612

### 613 **3.3.3. Wet water years**

614 The EoC wet WY is significantly wetter than all other WYs. Yet, unlike the historical WY,  
615 the precipitation largely comes as rain, as shown by the low-to-no snowfall and *SWE* totals (Figure  
616 6). The difference in future versus contemporary wet WY *SWE* (99%) is larger than the differences  
617 between the median and the dry WYs (91%). As in other WYs, soil moisture increases earlier  
618 compared to the historical wet WY. A greater water availability enables the system to meet the  
619 high EoC *ET* demand. Hence, *ET* in the EoC wettest year remains higher than the historical wettest  
620 year *ET* throughout the WY. However, the increase in *ET*, combined with the lack of snowmelt  
621 that can buffer and recharge soil moisture in spring, leads to less soil moisture at the end of the  
622 WY compared with the historical WY. Further, surface water storage increases earlier and at a  
623 much faster rate in the EoC WY compared to the historical WY. This is mirrored in the  
624 groundwater storages. As in the other EoC simulations, when compared to the historical  
625 counterpart the EoC wettest year shows a sharper decline in seasonal above and below groundwater  
626 storage changes (occurring between peak flow and baseflow). Groundwater storage decreases 47%  
627 in the EoC between peak flow and baseflow, whereas only a 41% decrease occurs in the historical

628 wet WY. Similarly, surface water storage decreases 44% in the EoC whereas only a 41% decrease  
629 occurs in the historical wet WY.

630

### 631 **3.4. Spatial patterns of the changes in fluxes and pressure-heads**

#### 632 **3.4.1. Median water years**

633 To provide a deeper understanding of how the changes in precipitation timing, magnitude,  
634 and phase affect the land surface processes and surface and subsurface hydrodynamic responses,  
635 we assess the spatial patterns of these changes during two key periods in the WY, peak flow and  
636 baseflow. Figure 7 shows the percent changes in *ET*, surface water pressure-heads, and subsurface  
637 pressure-heads (i.e., pressure-heads of the model bottom layer) in the EoC median WY compared  
638 to the historical median WY during peak flow and baseflow conditions (see the time frames in  
639 Figure 6). Regions in red correspond to areas with smaller fluxes or pressure-heads in the EoC  
640 compared to the historical ones, whereas regions in blue correspond to areas with larger fluxes or  
641 pressure-heads in the EoC compared to the historical median WY. We study peak flow and  
642 baseflow conditions because the analysis of the temporal variations of fluxes and storages has  
643 shown that these two periods are characterized by different trends and represent the key periods in  
644 understanding the hydrologic responses to the EoC extreme climate.

645 Relative to the historical median WY, during peak flow the EoC median WY is  
646 characterized by an increased *ET* across the majority of the watershed, especially in the Central  
647 Valley, and larger surface water and subsurface pressure-heads (Figure 7a-c). *ET* increases in the  
648 EoC both because of the increase in water availability and increased evaporative demand, as  
649 discussed in the previous section (3.3.1.). The increase in *ET* is non-uniform across the watershed  
650 because of the heterogeneity of the landscape's topographical gradients, land-surface cover, and

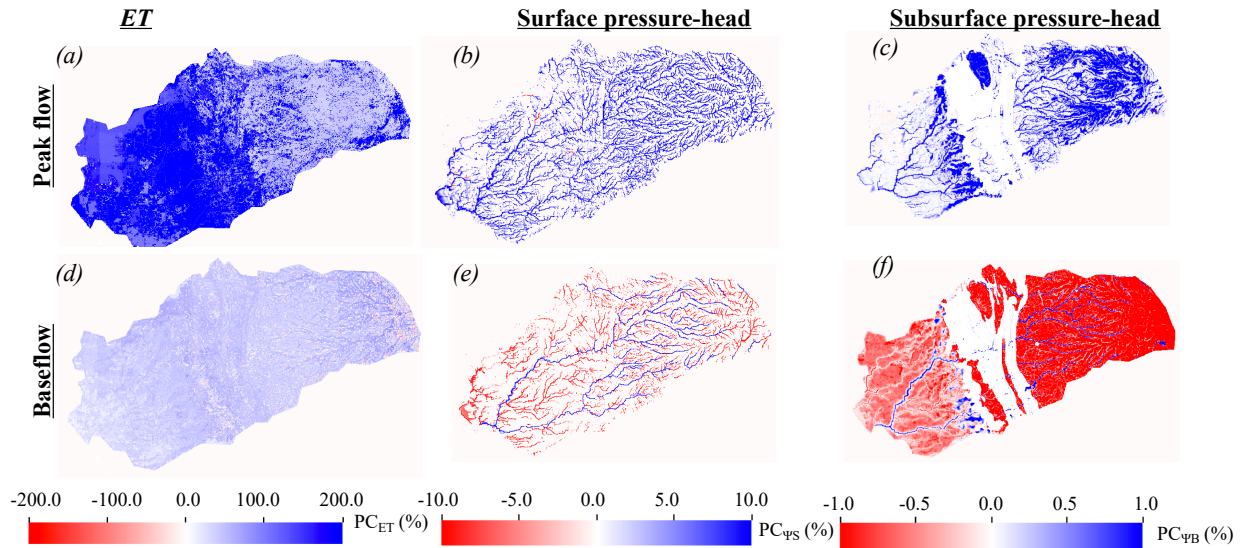


651 subsurface geological conditions. The Central Valley is characterized by a large increase in *ET*  
652 compared to the Sierra Nevada, and the patterns of *ET* in the Central Valley are also more  
653 homogeneous, a resultant of the geological characteristics of the area and the hydroclimate of the  
654 watershed (i.e., where most of the precipitation falls over the Sierra Nevada but follows  
655 topographic gradients downward into the valley where more recharge occurs). This leads to more  
656 water available in the Central Valley compared to the Sierra Nevada characterized by less  
657 permeable rocks. In addition, as most of the *ET* in the Central Valley comes from evaporation due  
658 to the high temperatures of the EoC (not shown here), the increase in evaporation is higher in the  
659 Central Valley due to its aquifers characterized by a high permeability (Maina and Siirila-  
660 Woodburn, 2020) and the availability of water.

661         Surface and subsurface pressure heads both show general increases during the EoC peak  
662 flow, yet these maps reveal that unlike *ET* the pressure head (and therefore storage) of water is  
663 very heterogeneous in space. For example, in the Sierra Nevada, we observe an increase in  
664 subsurface pressure-head (Figure 7c) only in some relatively permeable areas susceptible to  
665 infiltration and recharge. Although the Central Valley aquifers are more permeable and  
666 geologically less heterogeneous than the Sierra Nevada (as defined in the model), the changes in  
667 subsurface pressure-head in the Central Valley are heterogeneous. This is because the recharge of  
668 the Central Valley aquifers is dependent on the subsurface and surface flows from the headwater  
669 (i.e., connectivity to the headwater). In other words, only areas of the Central Valley that are  
670 subject to stronger connectivity with the headwaters see an increase in subsurface pressure-head  
671 in the EoC, likely because they are more regularly recharged by the headwaters through surface  
672 and subsurface flows from these areas, a recharge that buffers the water depletion through *ET*.

673 These are mostly the areas located close to the streams where there is an exchange between the  
674 subsurface and the surface and the Sierra Nevada foothills (in the alluvium 3 area, see Figure 1).

675 Relative to its historical counterpart, the EoC median WY is characterized by high *ET*  
676 during baseflow conditions though less than during peak flow conditions. (Figure 7d). We observe  
677 larger surface water pressure-heads in higher-order streams whereas surface water pressure-heads  
678 decrease in the EoC in the majority of the low-order, ephemeral streams (Figure 7e). This  
679 opposition of spatial pattern trends, resulting in more water in the main river channels, and less in  
680 the smaller streams, occurs for several reasons. First, peak flow occurs earlier in the EoC and is  
681 more rainfed, so that the ephemeral streams drain earlier in the EoC compared to in the historical  
682 period. This sustained and longer duration of draining increases the surface water pressure-head  
683 along the main river channels and is due to the contribution of the subsurface in the headwaters.  
684 This contribution is also higher in the EoC due to larger amounts of precipitation. The trends along  
685 the main river channel are also evident in the subsurface pressure-head maps (Figure 7f). Because  
686 the surface water is larger along the main channels, the subsurface pressure-heads are also larger  
687 here due to the interconnection between the subsurface and the surface (Figure 7f). However, in  
688 general, subsurface pressure-heads decrease elsewhere in the EoC during baseflow because of the  
689 lack of snowmelt and the higher *ET* demand. This result highlights the spatiotemporal complexity  
690 of an expected watershed's response to changes in climate (shown here to be bi-directional), and  
691 how factors such as river proximity may be crucial for consideration.



692  
 693 Figure 7: Comparisons between EoC median water year (WY) and the historical median WY peak  
 694 flow and baseflow spatial distributions of percent changes in  $ET$  ( $PC_{ET}$ ), surface water ( $PC_{\psi_S}$ ) and  
 695 subsurface ( $PC_{\psi_B}$ ) pressure-heads. Regions in red correspond to areas with smaller fluxes or  
 696 pressure-heads in the EoC compared to the historical ones, whereas regions in blue correspond to  
 697 areas with larger fluxes or pressure-heads in the EoC compared to the historical WY.

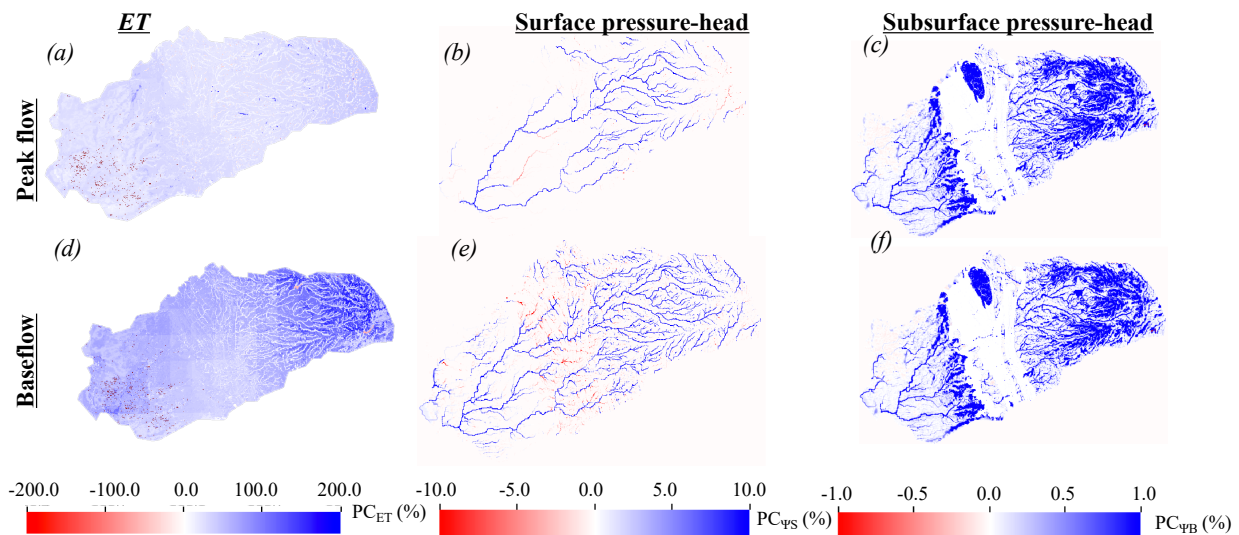
698

### 699 3.4.2. Dry water years

700 Figure 8 illustrates the percent changes in  $ET$ , surface water, and subsurface pressure-heads  
 701 in the EoC dry WY compared to the historical dry WY during peak flow and baseflow conditions.  
 702 During peak flow conditions, the EoC dry WY has larger  $ET$ , surface, and subsurface pressure-  
 703 heads than the historical dry WY (Figure 8a-c).  $ET$  is larger in this EoC dry WY not only because  
 704 it is hotter, but also because there is more precipitation, as noted previously. Increases in surface  
 705 pressure-heads are non-uniform across the domain. For example, surface water does not increase  
 706 in high elevation areas (i.e., elevation > 2000m) in the EoC dry WY because the change in the  
 707 precipitation phase is not significant. The main difference between the EoC and the historical dry

708 WY is the amount of the water flowing down gradient, which is higher in the EoC, hence the  
 709 surface water in the EoC becomes higher downstream. The increase in subsurface pressure-heads  
 710 in the EoC dry WY during peak flow conditions is heterogeneous with patterns similar to the  
 711 changes in subsurface pressure-heads associated with the EoC median WY.

712 During baseflow conditions, even though *ET* increases in the EoC driest WY relative to  
 713 the historical driest WY, surface, and subsurface pressure-heads also generally increase (Figure  
 714 8d-f). Given wetter conditions in the driest EoC WY, first-order streams are more pronounced. A  
 715 few low-order streams have less surface water in the EoC when compared to the historical dry  
 716 WY, similar to the results of the median WYs (see section 3.4.2). Subsurface pressure-head is  
 717 generally larger in areas subject to strong connectivity with the headwaters (i.e., receiving more  
 718 water from the headwaters through subsurface and surface flows) in the EoC dry WY relative to  
 719 the historical dry WY, with some regions experiencing no change from the historical conditions.  
 720 This suggests that the larger amount of precipitation associated with the EoC dry WY is sufficient  
 721 to supply enough water to account for high *ET* demands and recharge the groundwater.



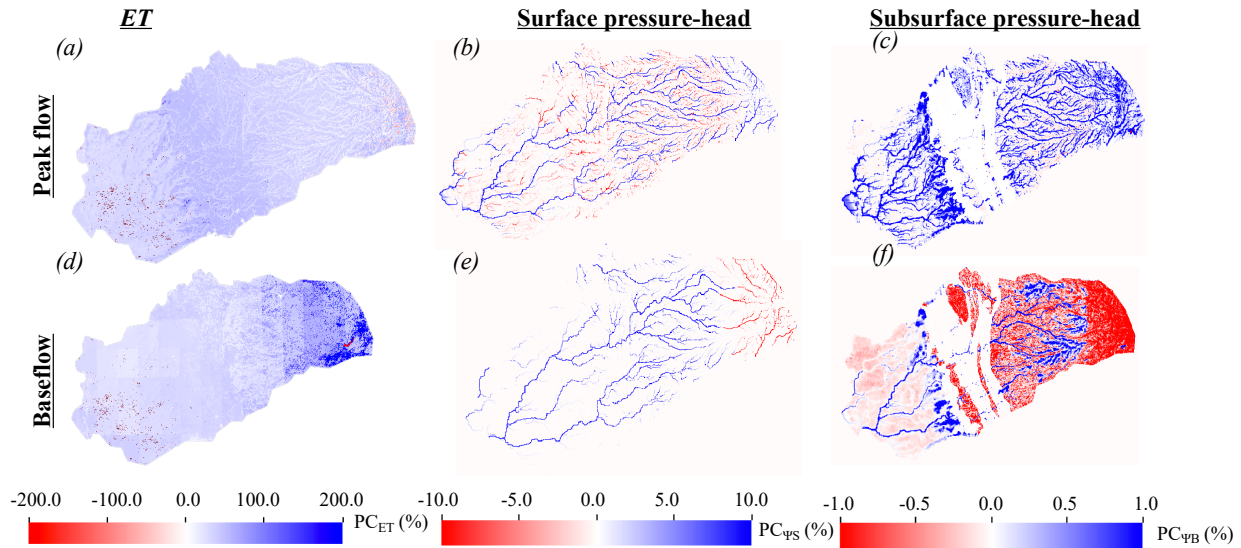
722  
 723 Figure 8: Comparisons between EoC dry water year (WY) and the historical dry WY peak flow  
 724 and baseflow spatial distributions of percent changes in *ET* ( $PC_{ET}$ ), surface water ( $PC_{\psi_S}$ ) and

725 subsurface ( $PC_{yB}$ ) pressure-heads. Regions in red correspond to areas with smaller fluxes or  
726 pressure-heads in the EoC compared to the historical ones, whereas regions in blue correspond to  
727 areas with larger fluxes or pressure-heads in the EoC compared to the historical WY.

728

### 729 **3.4.3. Wet water years**

730 Figure 9 shows the percent changes in  $ET$ , surface water, and subsurface pressure-heads in  
731 the EoC wet WY compared to the historical wet WY during peak flow and baseflow conditions.  
732 During peak flow, the EoC wet WY is characterized by larger  $ET$  and subsurface pressure-heads  
733 relative to the historical wet WY and a more heterogeneous mixture of regions with both higher  
734 and lower surface water conditions throughout the catchment (Figure 9 a-c). Analogous to other  
735 WYs at EoC, the surface water pressure-head increases (decreases) are apparent in larger-order  
736 (smaller order) streams, both in the Sierra Nevada and in the Central Valley. In the wettest WY,  
737 this occurs for several reasons. First, the larger volume of precipitation, plus seasonal shifts in  
738 precipitation timing result in the filling of the higher-order streams and depletion of the lower-  
739 order streams during peak flow. Second, in the historical wet WY, a significantly greater amount  
740 of snowpack is present in the Sierra Nevada in the upper elevation of the headwaters, allowing for  
741 slower, steadier amounts of water that is released during the spring via snowmelt, and in turn,  
742 supporting low-order streams over a longer period of time. The latter effect is immediately visible  
743 in Figure 9e, where decreases in EoC surface pressure heads are visible in the headwaters, despite  
744 the watershed-total showing an increase in EoC surface water storage during baseflow (see Figure  
745 6). Similar to the two previous EoC WYs, the subsurface pressure-head increases are shown more  
746 distinctly in the Central Valley during peak flow, under the main river channels, and in the foothills  
747 during baseflow (see previous sections on the discussion of hydroclimatic and geologic impacts).



748  
 749 Figure 9: Comparisons between EoC wet water year (WY) and the historical wet WY peak flow  
 750 and baseflow spatial distributions of percent changes in  $ET$  ( $PC_{ET}$ ), surface water ( $PC_{\psi_S}$ ) and  
 751 subsurface ( $PC_{\psi_B}$ ) pressure-heads. Regions in red correspond to areas with smaller fluxes or  
 752 pressure-heads in the EoC compared to the historical ones, whereas regions in blue correspond to  
 753 areas with larger fluxes or pressure-heads in the EoC compared to the historical WY.

754

#### 755 4. Discussion

##### 756 4.1 Comparison with previous studies

757 Some of the results presented in this study are qualitatively in agreement with previous  
 758 studies yet provide important new insights. For example, Maurer & Duffy, (2005) used 10 global  
 759 climate models to predict, as in this study, an increase in winter flows with an earlier peak flow  
 760 timing in the WY and a decrease in summer flows. Maurer & Duffy show that mid-century  
 761 projected annual precipitation and streamflow increases of 7% and 13% (respectively). Although  
 762 our study focused on EoC projections, we found that compared to the historical median WY,  
 763 annual surface water will increase by 19% in the EoC median WY. Compared to their findings,

764 our work sheds light on how these changes in runoff will occur across the watershed based on its  
765 physical characteristics and highlights that while runoff will increase in the EoC lower-order  
766 streams mainly located in the Sierra Nevada will see a decrease due to the change in the  
767 precipitation phase. Mallakpour et al., (2018) also had a similar finding in a study that shows that  
768 future California streamflow is altered similarly to Maurer & Duffy, (2005) under both the RCP4.5  
769 and RCP8.5 emissions scenarios, with RCP8.5 showing the highest changes during peak flow.  
770 However, contrary to our work the authors mentioned that the annual changes in streamflow will  
771 not be significant probably due to the compensation between increases in peak flow and decreases  
772 in baseflow. This was likely shaped by the differences in climate and hydrologic models used to  
773 derive these conclusions. Similar changes in streamflow were obtained by He et al., (2019) who  
774 drove the hydrologic model VIC with 10 global climate models to understand potential changes in  
775 runoff in California due to climate change. Hydrologic changes computed from the 10 global  
776 climate models were consistent and robust and showed an increase of around 10% in annual  
777 streamflow by the late century, a percentage similar to what has been found in this study. The  
778 authors mentioned that watershed characteristics such as geology, topography, and land cover  
779 strongly impact the hydrologic response to climate change. Relationships between watershed  
780 characteristics (e.g., physiographic parameters) and its responses to climate change were further  
781 explored by Son & Tague, (2019) who highlighted that because vegetation and subsurface geology  
782 control both water availability and energy demand, they in turn influence watershed sensitivity to  
783 a changing climate as shown in this study.

784         The increases in groundwater storage shown in this study are also in agreement with  
785 Niraula et al., (2017) who used the hydrologic model VIC to show that groundwater recharge will  
786 likely increase in the northern portion of the western United States in a changing climate. However,

787 contrary to their work that estimates changes in groundwater recharge over a large domain (i.e.,  
788 the western United States). In this work, we show that groundwater recharge decreases in the  
789 summer in some areas due to the lack of snowmelt and high EoC *ET*. Increases in *ET* in response  
790 to global warming were also documented by Pascolini-Campbell et al., (2021) who showed a 10%  
791 increase in global *ET* from 2003 to 2019.

792 An advantage of our approach is a more explicit estimate of spatiotemporal changes in  
793 groundwater-surface water feedbacks because Parflow-CLM physically solves the transfer and  
794 movement of water from the bedrock to the canopy. Additionally, the aforementioned studies used  
795 different emission scenarios and models to project changes in hydrology, nonetheless, their results  
796 have shown that the directions of the observed changes are consistent across models and emission  
797 scenarios and only the magnitude of these changes is uncertain. Hence, the trends observed in this  
798 study using a single model and emission scenario likely represent the trends we would observe  
799 using different models and scenarios. While our results show similar patterns and changes, our  
800 study provides a much finer-grained perspective on the sensitivity of a watershed to changes in  
801 climate extremes based on its subsurface geology, topography, and land cover. It also highlights  
802 that the spatiotemporal analyses of these changes may reveal different trends than if only assessed  
803 as annual changes. Understanding these localized changes and sensitivities is critical and has  
804 practical implications for water management.

805

#### 806 **4.2 Implications for water resources management**

807 Because our work provides a better understanding of the spatiotemporal changes in  
808 hydrodynamics in response to future extremes, our findings also have important implications for  
809 water resources in California. While previous work more broadly focused on how temperature



810 increases will alter the precipitation phase and reduce seasonal snowpack and increase winter  
811 runoff, this work brings new physical and more granular insights into how watersheds may respond  
812 to climate extremes. In particular, both wet and dry WYs in the future experience increased  
813 precipitation. As such, even in future dry WYs, water managers and stakeholders may need to  
814 prepare more for large precipitation events that may increase the possibility of flooding and require  
815 new infrastructure management strategies. For example, in a future where WYs are generally  
816 wetter, having alternatives for water supply during periods of sustained drought could be less  
817 important. However, as we show in this paper, shifts in precipitation timing, phase, and magnitude  
818 have cascading impacts on soil moisture profiles and *ET* withdrawals, which subsequently impact  
819 discharge and groundwater dynamics. Future shifts in water availability earlier in the year, as well  
820 as more dynamic transitions between peak and baseflow conditions (as quantified here), may  
821 impose stresses on water distribution, especially those systems already under scrutiny (e.g. those  
822 resources over-allocated or facing environmental degradation).

823         In addition, while these projections show increases in surface water and groundwater  
824 storages at watershed-scale, our results also highlight important localized spatiotemporal changes  
825 across a watershed, where the assumption of water storage increase does not necessarily hold in  
826 all geographic locations (e.g., areas that are not close to the river in the Central Valley). Our study  
827 also shows that the decreases in groundwater storage in the Central Valley aquifers are more  
828 significant than the decreases in surface water storage during baseflow conditions. This may call  
829 for new conveyance infrastructure that can move water from the relatively wetter areas to the drier  
830 areas and/or where infiltration can more readily occur. The latter suggests solutions such as  
831 Managed Aquifer Recharge (MAR) could become an increasingly important climate change  
832 adaptation. Finally, our study also highlights that lower-order streams will likely become more

833 ephemeral in the EoC due to flashier runoff and higher evaporative demand, such conditions will  
834 have important implications for fish spawning and ecosystem nutrient cycling. Although our  
835 results are embedded with uncertainties and are based on a single projection and model, they do  
836 highlight the need for a revisitation of current water management strategies. Further studies using  
837 different climate and land-use scenarios and models of varying complexity and resolution could  
838 help build more confidence and provide more information in defining how future water  
839 management strategies would need to change to be more resilient to more extreme WYs in the  
840 future.

841

#### 842 **4.3 Study limitations**

843 This study combines novel climate and hydrologic simulations that provide both  
844 advantages and disadvantages compared with previous work (He et al., 2019; Maurer & Duffy,  
845 2005; Niraula et al., 2017; M. Safeeq et al., 2014; Son & Tague, 2019). We note several of these  
846 disadvantages below. In the integrated hydrologic model, the subsurface geology and land cover  
847 characterization has inherent and, in some cases, irreducible uncertainty. This study uses  
848 hydrodynamic parameters as defined by Maina et al. (2020a), which assumes that the subsurface  
849 hydrodynamics from the Sierra Nevada to the Central Valley is almost completely hydrologically  
850 separated except through overland flow. However, it is not clear whether fractures or other  
851 macrostructures may drive more surface and subsurface flows from the headwaters to the Central  
852 Valley aquifers. In addition, we use the historical land surface cover map when simulating the  
853 EoC. Since vegetation will dynamically respond to a changing climate, the land surface cover used  
854 in the EoC simulations may be unrealistic and may influence, for example, *ET* and/or soil moisture.  
855 For example, it has been shown that the stomatal resistance of plants will change due to rising CO<sub>2</sub>

856 with important implications for both the water and energy balance (Lemordant et al., 2018; Milly  
857 & Dunne, 2017). Yet, our use of historical land surface cover does have the advantage of isolating  
858 changes in fluxes associated with climate change alone and could be compared in future work with  
859 additional simulations that account for both changes in the land surface and climate. Future studies  
860 will assess the impact of changes in vegetation physiology and land surface cover on watershed  
861 hydrodynamics. In this study, we did not include the impacts of anthropogenic activities such as  
862 pumping and irrigation due to the uncertainties in predicting these fluxes in EoC. While these  
863 human interventions could substantially change the hydrologic system, our study isolates the  
864 impacts of a changing climate on the natural system. Future studies can now estimate the impacts  
865 of different pumping and irrigation scenarios at EoC that may further impact the hydrologic system  
866 hydrodynamics in a changing climate and compare and contrast with this work. Although our VR-  
867 CESM simulations represent a cutting-edge global climate model simulation (e.g., 28 km regional  
868 grid-refinement, coupled atmosphere-land simulation with prescribed ocean conditions, etc.),  
869 further work may be needed to evaluate how a more refined grid resolution impacts atmospheric  
870 process representation over the Cosumnes watershed, particularly in the headwaters (Maina et al.,  
871 2020b). We further acknowledge that the 30-year simulation may not be sufficient to capture  
872 certain climate extremes (e.g., 1-in-50-year storm). Future studies, if computational resources are  
873 available, will seek to explore how the use of a longer time period might influence the  
874 identification of the most extreme dry and wet WYs from VR-CESM.

875         In this study, we relied on deterministic models to represent both the atmospheric (VR-  
876 CESM) and hydrologic (ParFlow-CLM) dynamics. These models are very sensitive to the initial  
877 conditions and input parameters (La Follette et al., 2021; Lehner et al., 2020; Song et al., 2015)  
878 which are uncertain given the lack of data characterizing the above and below-ground

879 environment, including its hydrological response. Thus, while it is important to assess the  
880 sensitivity of the model outputs to these uncertain parameters, these models are computationally  
881 expensive and require many parameters. For example, a complete sensitivity analysis of the  
882 hydrologic model requires running it thousands of times to explore the full parameter space (which  
883 has a dimension of over 29). Such an approach is not feasible with the currently available  
884 computational resources because it takes longer than one wall-clock day to simulate a single water  
885 year for a single model parameterization, even in a high-performance computing environment.  
886 Future work could employ reduced order models based on a subset of the physics-based model  
887 runs to explore parameter space further (e.g. Maina et al., 2022). In addition, because of the  
888 behavior of hydrological processes, the climate variability, and the uncertainties of deterministic  
889 models, model validation should ideally be performed over a long period to account for different  
890 changes and variabilities. In this study, model validation was limited to a period of 5 years due to  
891 computational constraints. Although this period encompasses the wettest and driest years on record  
892 in the region, we acknowledge that it may not be sufficient to capture the full range of hydrological  
893 variability. Another limitation of using deterministic models is that the temporal variations of  
894 hydrological processes tend to follow a stochastic behavior in accordance with the so-called Hurst  
895 phenomenon (Hurst, 1951; Koutsoyiannis, 2003). As a result, the use of deterministic models such  
896 as the ones employed in this study could intensify the impacts of hydrological extremes and climate  
897 change. Finally, it has also been demonstrated that while the changes in water balance exhibit  
898 greater variability on climatic scales, the most important changes in hydrologic processes remain  
899 the overexploitation of groundwater (Ferguson and Maxwell, 2010) which has an impact on the  
900 rise in sea level (Koutsoyiannis, 2020). In addition to projecting the use of groundwater by the end

901 of the century, future studies could compare the two approaches (deterministic and stochastic) to  
902 better assess the limitations and the uncertainties associated with them.

## 903 **5 Summary and Conclusions**

904 The effects of climate change are increasingly felt across many regions of the world,  
905 especially in hydrologically sensitive regions with Mediterranean climates such as California.  
906 Many studies over the years have been conducted to better understand the hydroclimate of the EoC  
907 and its impacts on the hydrologic cycle. Previous studies have used a multitude of different models  
908 at varying complexity and climate scenarios to highlight that the future climate has multiple  
909 plausible outcomes. Most of these studies indicate warmer temperatures and precipitation that  
910 mostly falls as rain instead of snow. For example, the state of California is projected to experience  
911 more punctuated climate extremes coupled with a marked decrease in the Sierra Nevada snowpack  
912 (Cayan et al., 2008; Gleick, 1987; Musselman, Molotch, et al., 2017; Rhoades, Ullrich, &  
913 Zarzycki, 2018). Such drastic transitions have already started to shape the hydroclimate of  
914 California. Faced with this new normal, it is becoming increasingly important to assess how the  
915 integrated hydrologic cycle may respond to these perturbations and connect these responses more  
916 directly to water resource management, particularly with modeling frameworks that can better  
917 represent the interactions between the changing atmosphere and the surface and subsurface  
918 hydrology.

919 In this work, we used state-of-the-art physics-based models at high resolutions for their  
920 respective communities to project changes in meteorological conditions at the EoC and assess how  
921 their combined effects influence watershed hydrology from the land surface to the deeper  
922 subsurface. Importantly, our approach to couple a variable resolution Earth System Model and an  
923 integrated hydrologic model allow for us to simulate hydro-meteorological conditions which are

924 jointly driven by thermodynamical and dynamical shifts in climate. We model the Cosumnes  
925 watershed, which spans the Sierra Nevada and Central Valley and hosts one of the last rivers in  
926 the state without a large dam, as a testbed to understand how climate drivers will impact water  
927 resources in the EoC. We performed climate simulations over 30-year periods historically (1985-  
928 2015) and at EoC (2070-2100) and identified the driest, median, and wettest WYs from those  
929 simulations, which were then used as meteorological forcing for the hydrologic model. Our  
930 coupled simulations project that, for the Cosumnes watershed, temperature and precipitation will  
931 both increase by the EoC across all WY types (wettest, median, and driest). In addition,  
932 precipitation is projected to fall earlier compared to historical conditions and mainly in the form  
933 of rain. For the median and wet WYs the precipitation season has earlier cessation dates, while the  
934 dry EoC WY, which is wetter than its historical counterpart, persists significantly longer into the  
935 spring. As a consequence of warmer temperatures, all WYs show a substantial decrease in *SWE*.  
936 The shift of precipitation from snowfall to rainfall, as well as the increase in the amount of  
937 precipitation and the early start of precipitation lead to an overall increase in soil moisture and  
938 more water available to meet the higher EoC *ET* demand. Importantly, this increase in *ET* is  
939 heterogeneous across the watershed and highlights one of the main advantages of using an  
940 integrated hydrologic model such as the one we employed in this study to assess the spatiotemporal  
941 patterns of change. Our results show that the sensitivity to the changes in *ET* at EoC depends on  
942 the subsurface geology and topographical gradients. More specifically:

- 943 • The geological and topographical complexities of the Sierra Nevada headwaters  
944 lead to highly heterogeneous changes in *ET*. Changes in *ET* are higher in permeable  
945 areas such as the plutonic rocks where water can be more easily extracted.

946           • *ET* changes in the Central Valley of the Cosumnes watershed are predominantly  
947           uniform with the highest sensitivities in the vicinity of the Cosumnes River due to  
948           the high availability of water.

949           Precipitation increases enough in the EoC to provide water for both increased *ET* and  
950           increased surface water storage. Surface water storages also increase earlier in the WY and have  
951           higher peak amounts. This earlier and larger increase is a direct consequence of an earlier start in  
952           precipitation at EoC, a marked change in the precipitation phase, and an overall larger amount of  
953           precipitation when compared with the historical WYs. However, our results also highlight that  
954           during baseflow conditions surface water decreases, especially in lower-order streams, showing  
955           that these areas are highly sensitive to the change in precipitation phase. Our simulations also show  
956           that the seasonal variability of the EoC watershed behavior is also more dynamic. In general,  
957           decreases in seasonal water storages occurring between peak flow and baseflow conditions are  
958           more than 10% higher in the EoC compared to the historical conditions.

959           EoC groundwater storages are also projected to increase earlier in the WY with peaks  
960           greater than those found historically. Yet these storages decrease significantly during baseflow  
961           conditions due to the higher *ET* at EoC and the absence of recharge from snowmelt. Contrary to  
962           the changes in surface water storages, groundwater storages show a larger decrease due to their  
963           dependence on the surface water from the Sierra Nevada. Our results also show that changes in  
964           subsurface pressure-heads are not uniform and are bi-directional throughout the Cosumnes  
965           watershed. Because the connectivity between the Central Valley aquifers and the Sierra Nevada  
966           headwaters (i.e., subsurface and surface flows from the headwater to the Central Valley aquifers)  
967           plays an important role in the hydrodynamics of this watershed, only areas with a strong connection  
968           with the headwaters, such as the foothills and the river channels, see an increase in subsurface

969 pressure-heads at EoC. However, the subsurface pressure-heads decrease elsewhere in the Central  
970 Valley aquifers especially in baseflow conditions due to the high *ET* and the lack of snowmelt. In  
971 the river channels, this is due to the exchange between the subsurface and the surface whereas the  
972 foothills characterized by the consolidated sediments serve as “spillover.”

973         Our results provide novel understandings about possible changes in the integrated  
974 hydrologic response to changes in EoC climate extremes. An important caveat is that our  
975 simulation was a single set of climate realizations and may not properly bound internal variability  
976 uncertainty like an ensemble of climate simulations could. However, beyond the widely agreed-  
977 upon changes of decreased snowpack and shifts in runoff timing in the literature, we show that in  
978 this simulation: 1) EoC precipitation increases even in the driest years; 2) despite an increased  
979 temperature, and hence *ET*, both groundwater and surface water storage increase relative to  
980 historical conditions because of increased precipitation; and 3) there is a distinct spatial pattern,  
981 particularly in surface water storage, in which smaller-order streams see reduced flow while the  
982 larger order streams see an increased flow. These changes will have strong implications on natural  
983 resource management.

984         In this study, land cover changes are assumed to not occur, however, changes in land cover  
985 are expected to occur in the future, either naturally or anthropogenically. Further vegetation  
986 physiology will also change in response to an increase in CO<sub>2</sub>. Thus, future studies should  
987 investigate the impacts of these changes and how they may further alter the integrated hydrologic  
988 budgets. Additionally, future studies could also assess the effects of anthropogenic activities such  
989 as pumping and irrigation under a changing climate, other emissions scenarios, and/or the  
990 sequencing of variable end-member WYs and the interannual memory of the hydrologic system.  
991 Importantly, an understanding of this variability could be used to inform how water managers

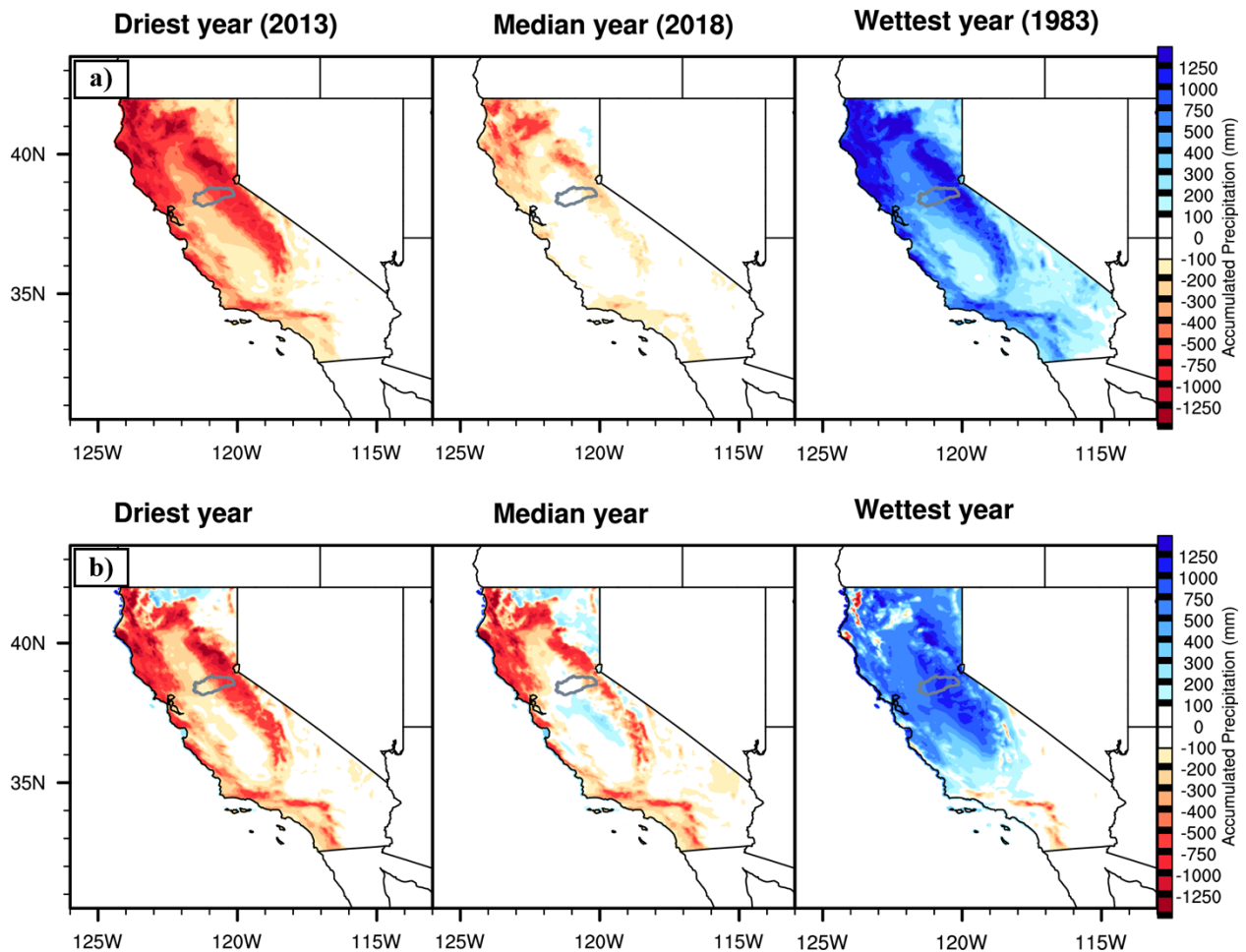


992 might prepare for more intense and/or intermittent extremes in the future. Future research could  
993 also use multiple emission scenarios to better assess the range in hydrodynamic responses  
994 dependent on the severity of climate change, especially those related to the magnitude and spatial  
995 location of the precipitation response since they are likely more uncertain and scenario-dependent  
996 than the trends at the watershed-scale.

997 **Appendix A: Comparisons between VR-CESM and PRISM historical conditions**

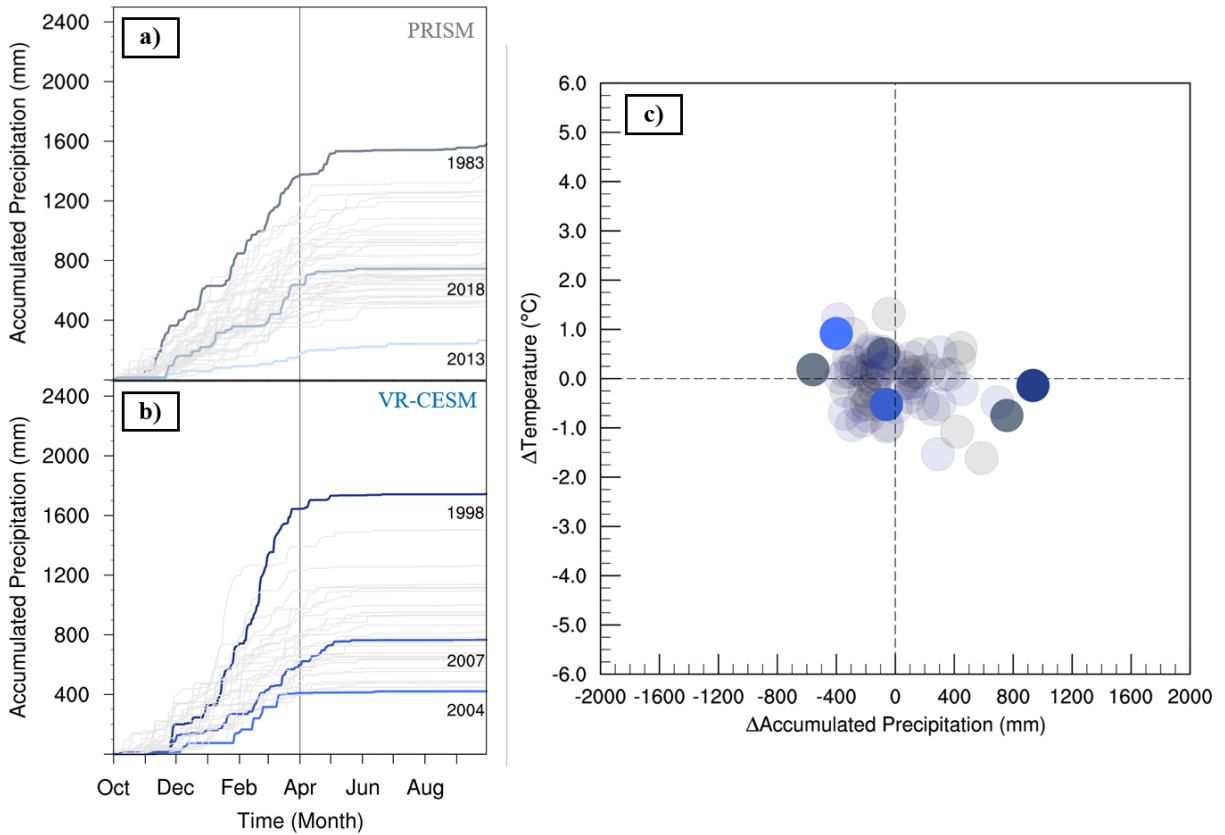
998 Figure A1 highlights differences in dry, median, and wet WY accumulated precipitation  
999 relative to the 1981-2019 PRISM climatology. VR-CESM generally recreates the spatial pattern  
1000 of anomalous dry and wet patterns across California for each WY type. This is shown via the  
1001 common regions of minimum and maximum anomalies relative to the PRISM climatology.  
1002 Notably, there are regions where VR-CESM anomalies are not consistent with PRISM. This is  
1003 primarily shown in the wettest water year in portions of the Central Valley, western slopes of the  
1004 Sierra Nevada, and southern California. This is likely correlated with resolution and the lack of  
1005 orographic gradients (both valleys and peaks) in VR-CESM at 28km resolution. Mismatches in  
1006 accumulated precipitation may also be due to representation of atmospheric rivers (ARs) in VR-  
1007 CESM that were found to be generally larger, slightly more long-lived and make landfall more  
1008 frequently over California (Rhoades et al., 2020b). Figure A2 shows Cosumnes watershed WY  
1009 accumulated precipitation and surface temperature. WY accumulated precipitation is shown in  
1010 Figure A 2a and 2b for PRISM and VR-CESM, respectively. All WY accumulated precipitation  
1011 simulated by VR-CESM over 1985-2015 are within the range in PRISM, save for the wettest WY.  
1012 This is shown more explicitly in quadrant space in Figure A2c where the range of annual bias in  
1013 VR-CESM relative to the range of interannual variability in PRISM for accumulated precipitation  
1014 and temperature is shown. VR-CESM generally simulates a wetter historical period over the  
1015 Cosumnes (range of bias of 1330 mm) relative to PRISM (range of interannual variability of 1320  
1016 mm). Basin-average minimum (421 mm) and maximum (1740 mm) WY accumulated  
1017 precipitation are slightly larger than is found in PRISM. Of relevance to this study, PRISM has  
1018 shown notable uncertainties in the Sierra Nevada. Lundquist et al., 2015 showed that an  
1019 underrepresentation of the most extreme storm total precipitation in the Sierra Nevada can result

1020 in an upper-bound uncertainty of 20% in WY accumulated precipitation. Therefore, the wettest  
1021 WY of VR-CESM is well within the 20% uncertainty range of PRISM's wettest WY ( $1580 \pm 316$   
1022 mm). Further, differences in basin-average WY accumulated precipitation between VR-CESM  
1023 and PRISM are non-significant using a t-test and assuming a p-value  $< 0.05$ . The range of  
1024 temperature bias in VR-CESM ( $2.74\text{ }^{\circ}\text{C}$ ) relative to the range of PRISM interannual variability  
1025 ( $2.93\text{ }^{\circ}\text{C}$ ) was also within the temperature uncertainties discussed in Strachan and Daly, 2017.  
1026 They showed that a general cool-bias in PRISM temperatures were found on the leeward side of the  
1027 Sierra Nevada when compared with 16 out-of-sample in-situ observations across an elevation  
1028 gradient of 1950 to 3100 meters with an overall mean bias of  $-1.95\text{ }^{\circ}\text{C}$  (maximum temperature)  
1029 and  $-0.75\text{ }^{\circ}\text{C}$  (minimum temperature).



1030

1031 Figure A1: Differences in the driest, median, and wettest water year accumulated precipitation  
1032 over California in a) PRISM and b) VR-CESM relative to the 1981-2019 PRISM climatology.  
1033 The Cosumnes watershed boundary is outlined in gray.

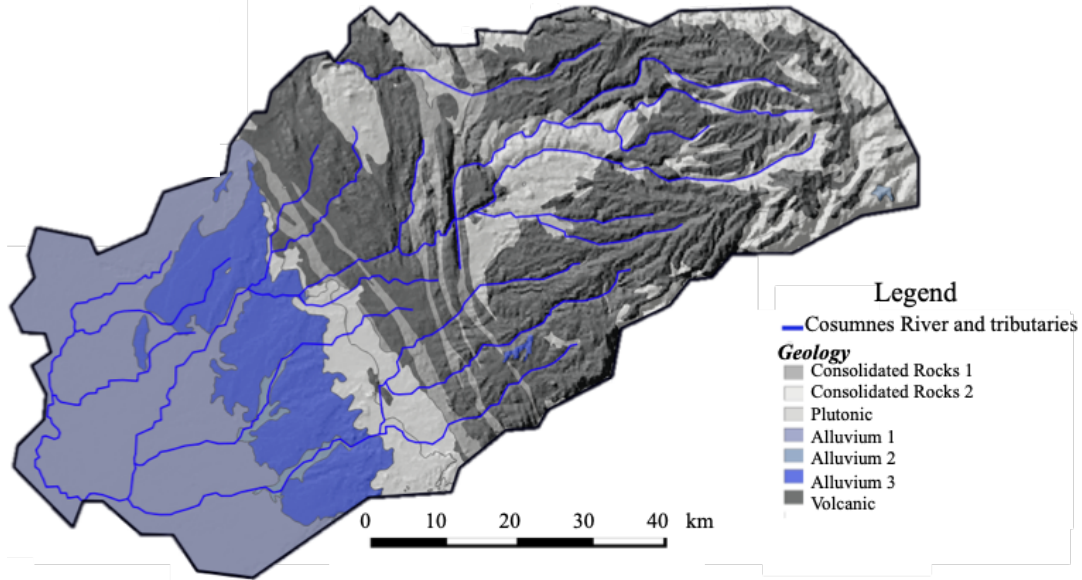


1034  
1035 Figure A2: Cosumnes watershed accumulated precipitation totals in a) PRISM (gray; 1981-2019)  
1036 and b) VR-CESM (blue; 1985-2015) with dry, median, and wet years emboldened. c) shows  
1037 differences in PRISM (gray) and VR-CESM (blue) relative to the PRISM climatology (1981-2019)  
1038 in temperature and accumulated precipitation quadrant space. Dry, median, and wet water years  
1039 are emboldened.

1040  
1041

1042 **Appendix B: Integrated Hydrologic Model Parameterization**

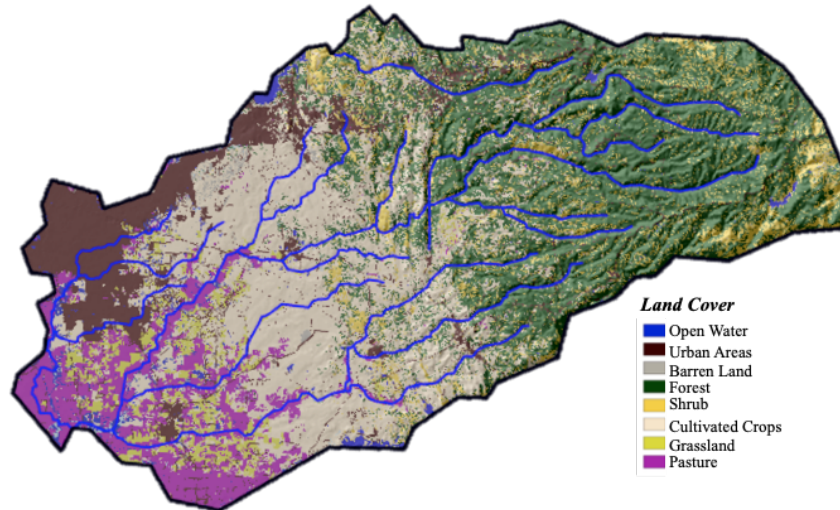
1043 **1. Input Variables**



1044 Figure B1: Geological map of the Cosumnes watershed (source: USGS, Jennings et al., 1977)  
 1045  
 1046

<b>Hydrodynamic properties based on the geology</b>				
Geological Formation	Porosity (-)	Specific Storage ( $m^{-1}$ )	Van Genuchten $\alpha$ ( $m^{-1}$ )	Van Genuchten $n$ (-)
Bedrock (Consolidated, Plutonic and Volcanic Rocks)	0.02	$10^{-6}$	3.0	3.0
Alluvial aquifers	0.2	$10^{-4}$	3.0	3.0

1047 Table B1: Assigned values of hydrodynamic parameters (porosity, specific storage and Van  
 1048 Genuchten parameters). Values are based on literature review (Faunt et al., 2010; Faunt and  
 1049 Geological Survey (U.S.), 2009; Flint et al., 2013; Gilbert and Maxwell, 2017; Welch and Allen,  
 1050 2014).



1051 Figure B2: Cosumnes watershed characteristics: land use and land cover (source: Homer et al.,  
 1052 2015), and model boundaries.  
 1053  
 1054

Surface roughness based on land use			
Land Use	Manning Coefficient ( $\text{h.m}^{-1/3}$ )		
Forest	$5 \times 10^{-2}$		
Shrub land and agricultural area	$5 \times 10^{-3}$		
Urban areas	$5 \times 10^{-5}$		
Crop properties			
Crop Type and Reference	Height (m)	Maximum Leaf Area Index (-)	Minimum Leaf Area Index (-)
Alfalfa (Evelt et al., 2000; Orloff, 1995; Robison et al., 1969)	0.6	6.0	2.0
Pasture (Buermann et al., 2002; King et al., 1986; Rahman and Lamb, 2017)	0.12	6.0	1.0
Vineyards (Johnson and Pierce, 2004; Vanino et al., 2015)	0.9	3.0	0.6

1055 Table B2: Manning coefficients and crop properties  
 1056

Boundary conditions	Value
Mokelumne and American river	Weekly-varying Dirichlet boundary conditions. These values are based on the measured river stages.
Sierra Nevada limit	No flow Neumann boundary condition
Bottom of the model	No flow Neumann boundary condition

1057 Table B3: boundary conditions  
 1058  
 1059  
 1060

## 2. Numerical model set-up

1061

Domain size	~7000 km <sup>2</sup>								
Spatial discretization	200 m horizontal from 0.1 m to 30 m in the vertical direction								
	Vertical Resolution								
	Layer	1	2	3	4	5	6	7	8
$\Delta z(m)$	0.1	0.3	0.6	1.0	8.0	15.0	25.0	30.0	
Simulation time	Model validation (from water year 2012 to water year 2017), then future water years								
Temporal discretization	hourly								

1062 Table B4: Numerical model discretization

1063

1064

1065

### 3. Output variables

Selected output variables	Temporal scale	Spatial scale
Snow Water Equivalent	Yearly, monthly, and hourly	Domain-average and point scale
Evapotranspiration	Yearly, monthly, and hourly	Domain-average and point scale
Soil Moisture	Yearly, monthly, and hourly	Domain-average and point scale
River Stages (also surface water storages)	Yearly, monthly, and hourly	Domain-average and point scale
Groundwater levels variations (also subsurface storages)	Yearly, monthly, and hourly	Domain-average and point scale

1066 Table B5: Selected output variables

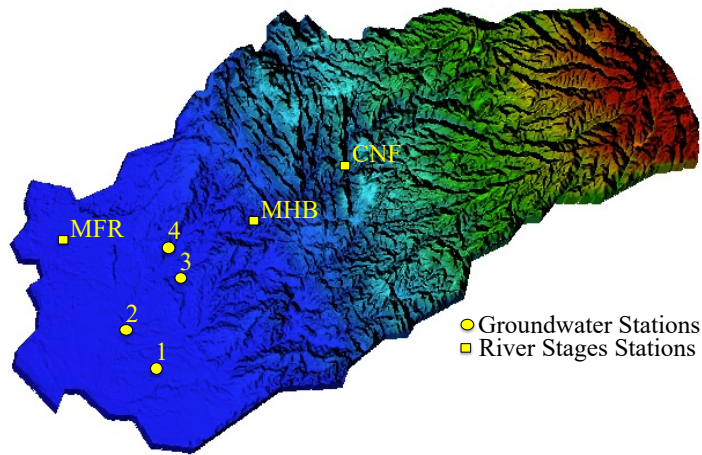
1067

1068

1069

1070 **Appendix C: Integrated Hydrologic Model Validation**

1071 We compared temporal variations of streamflow at 3 stations located in the Sierra  
1072 (uplands), the intersection between the Sierra and the Central Valley, and the outskirts of  
1073 Sacramento (see Figure C1). Four wells in the watershed (see Figure C1) have reasonable, publicly  
1074 available records of groundwater levels and were used to check the ability of the model to  
1075 reproduce water table depth variations.



1076  
1077 Figure C1: The locations of the 3 streamflow gauges (CNF, MHB, and MFR) and 4  
1078 groundwater wells (stars).

1079  
1080 Figure C2a depicts the comparisons between simulated and measured river stages at the 3  
1081 stations indicated in figure C1. Absolute errors (L1) in m and relative errors (L2) are shown in  
1082 Table C1. Differences between simulated and measured streamflow vary between 0.4 and 0.8 m  
1083 (Table C1) indicating that the model is able to reproduce the river dynamics.

1084 Absolute differences given by:

1085 
$$L_{1i,j} = |X_{mes_{i,j}} - X_{sim_{i,j}}| \tag{C1}$$

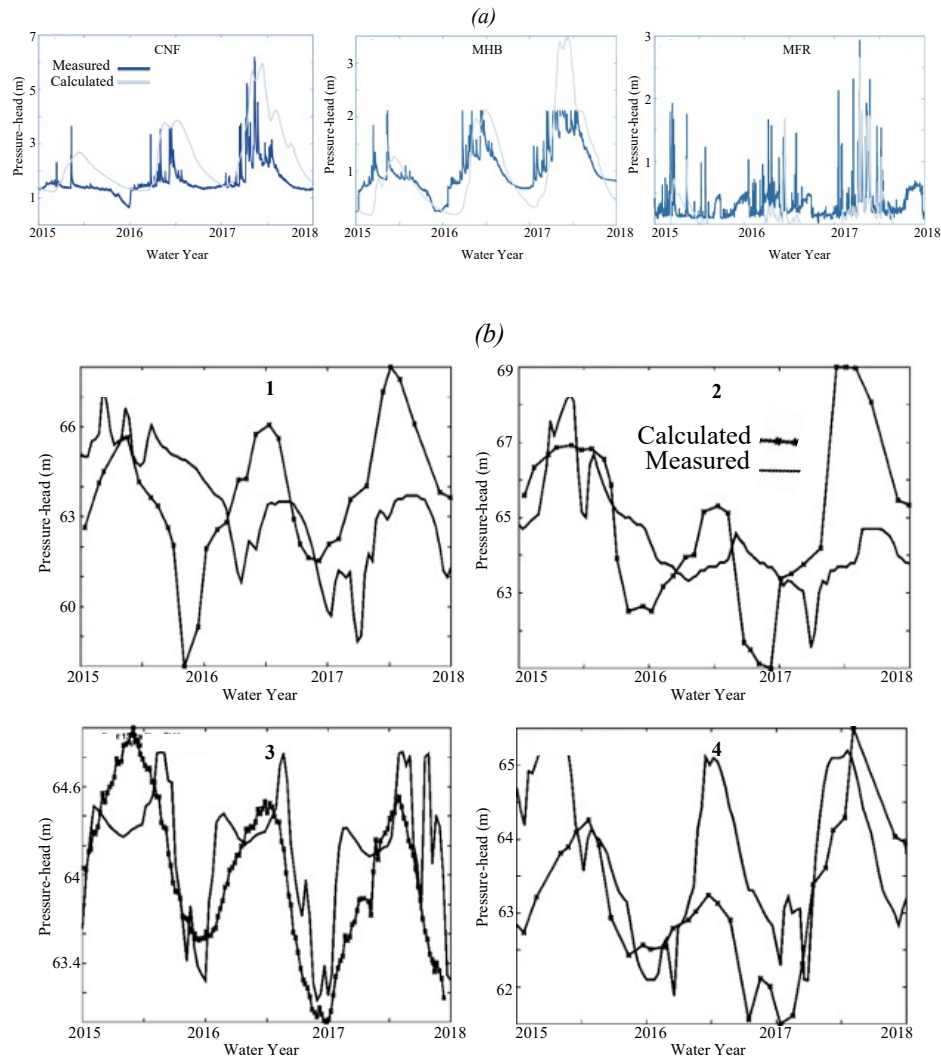


1086 Where  $L_{1,i,j}$  is the absolute difference associated with cell  $i$  and time  $j$ ,  $X_{mes_{i,j}}$  is the  
 1087 measured (or remotely sensed) data, and  $X_{sim_{i,j}}$  the simulated value.

1088 Relative differences  $L_{2,i,j}$  are given by:

1089 
$$L_{2,i,j} = \frac{|X_{mes_{i,j}} - X_{sim_{i,j}}|}{X_{mes_{i,j}}} \quad (C2)$$

1090



1091  
 1092 Figure C2: Comparisons between measured and calculated (a) river stages (i.e., pressure-  
 1093 heads simulated by ParFlow-CLM) and (b) subsurface pressure-head. The location of the selected  
 1094 points is indicated in Figure C1.

1095

<b>Measurements</b>	<b>L<sub>1</sub> (m)</b>	<b>L<sub>2</sub> (-)</b>
River Stages (CNF)	0.8	0.5
River Stages (MHB)	0.4	0.36
River Stages (MFR)	0.57	1.06
Groundwater Levels (Well 1)	3.73	0.05
Groundwater Levels (Well 2)	1.63	0.02
Groundwater Levels (Well 3)	0.476	0.0077
Groundwater Levels (Well 4)	1.08	0.016

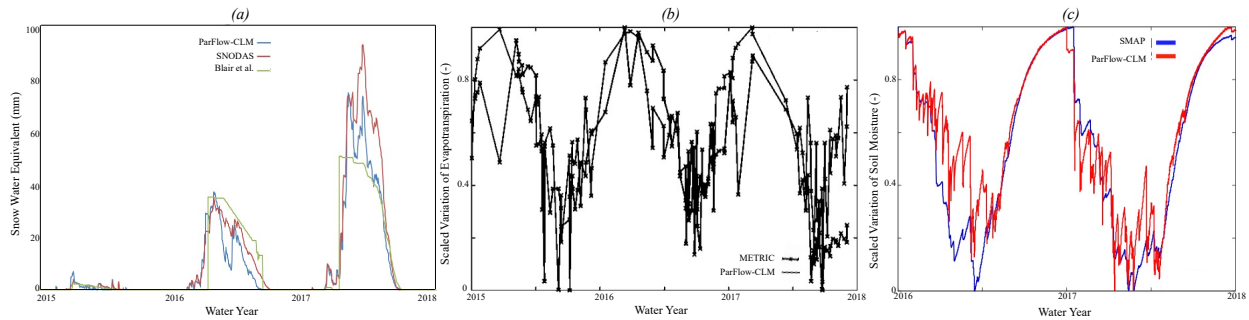
1096 Table C1: Differences between measured and calculated surface and groundwater levels. L<sub>1</sub> is the  
1097 absolute error and R<sub>2</sub> the relative error.

1098

1099 Comparisons between simulated and calculated groundwater levels (here referred to as the  
1100 pressure-heads at the bottom of the domain) shown in Figure C2b indicate that the model has  
1101 reasonable agreements with measurements. As shown in table C1, the error varies between 0.47 to  
1102 3.73 m depending on the station. Mismatches between simulated and observed groundwater levels  
1103 at wells 1 and 2 are likely due to an inaccurate estimation of pumping in these areas. The temporal  
1104 variations of the groundwater levels show an impact of withdrawals but because these withdrawals  
1105 are hard to estimate the model isn't correctly reproducing these trends.

1106 ParFlow-CLM also solves the key land surface processes governing the transfer of water  
1107 and energy at the land-atmosphere-soil interface: evapotranspiration, snow dynamics, and soil  
1108 moisture. In Maina et al., (2020a), rigorous comparisons between the ParFlow-CLM simulated  
1109 land surface processes and remotely sensed estimates of these variables were conducted (Figure

1110 C3). Table C2 shows the correlation coefficient between ParFlow-CLM results and the various  
 1111 datasets compared.



1112  
 1113 Figure C3: (a) Comparisons between domain-averaged total snow water equivalent obtained with  
 1114 ParFlow-CLM, SNODAS and Bair et al., reconstruction, (b) Comparisons between actual  
 1115 evapotranspiration obtained with ParFlow-CLM and METRIC (c) Relative variation of soil  
 1116 moisture obtained with ParFlow-CLM and SMAP. Note that the x-axis of (c) is shorter because of  
 1117 the availability of SMAP data

Satellites based products	L <sub>1</sub> (m)	L <sub>2</sub> (-)	Pearson Correlation Coefficient
SWE SNODAS (mm)	3.09	3.77	0.97
SWE Bair et al., (mm)	3.80	2.69	0.84
Soil Moisture SMAP (-)	0.217	3.07	0.94
ET METRIC (mm/s)	0.067	1.40	0.6

1118 Table C2: differences between measured and remotely sensed evapotranspiration (METRIC), soil  
 1119 moisture (SMAP), and snow water equivalent (SNODAS and Bair et al., 2016)

1120

1121 **Data availability**

1122 Data supporting the findings of this study can be found here:

1123 <https://portal.nersc.gov/archive/home/a/arhoades/Shared/www/Hyperion/>

1124 **Author contribution**

1125 The authors contribute equally to this work.

1126 **Competing interests**

1127 The authors declare that they have no conflict of interest.

1128 **Acknowledgements**

1129 Fadji Zaoua Maina and Erica Siirila-Woodburn were supported by LDRD funding from Berkeley  
1130 Lab, provided by the Director, Office of Science, of the U.S. Department of Energy under Contract  
1131 No. DE-AC02-05CH11231.

1132 Author Alan M. Rhoades was funded by the Department of Energy, Office of Science Office of  
1133 Biological and Environmental Research program under Award Number DE-SC0016605 "A  
1134 framework for improving analysis and modeling of Earth system and intersectoral dynamics at  
1135 regional scales" and Award Number DE-AC02-05CH11231 "The Calibrated and Systematic  
1136 Characterization, Attribution, and Detection of Extremes - Science Focus Area".

1137 This research used computing resources from the National Energy Research Scientific  
1138 Computing Center, a DOE Office of Science User Facility supported by the [http://](http://dx.doi.org/10.13039/100006132)  
1139 [dx.doi.org/10.13039/100006132](http://dx.doi.org/10.13039/100006132) of the U.S. Department of Energy under Contract No. DE-  
1140 AC02-05CH11231.

1141  
1142  
1143

1144           **References**

- 1145   Abbott, M. B., J. C. Bathurst, J. A. Cunge, P. E. Oconnell, and J. Rasmussen (1986), An  
1146           introduction to the european hydrological system: Sys- teme hydrologique Europeen, She  
1147           .2. Structure of a physically-based, distributed modeling system, *J. Hydrol.*, 87(1–2), 61–  
1148           77.
- 1149   Allan, R.P., Barlow, M., Byrne, M.P., Cherchi, A., Douville, H., Fowler, H.J., Gan, T.Y.,  
1150           Pendergrass, A.G., Rosenfeld, D., Swann, A.L.S., Wilcox, L.J. and Zolina, O. (2020),  
1151           Advances in understanding large-scale responses of the water cycle to climate change.  
1152           *Ann. N.Y. Acad. Sci.*, 1472: 49-75. <https://doi.org/10.1111/nyas.14337>
- 1153   Allen R. G., Masahiro T., Ricardo T. (2007) Satellite-based energy balance for mapping  
1154           evapotranspiration with internalized calibration (METRIC)—model *J. Irrig. Drain.*  
1155           *Eng.*, 133, pp. 380-394, 10.1061/(ASCE)0733-9437(2007) 133:4(380).
- 1156   Alo, C. A., & Wang, G. (2008). Hydrological impact of the potential future vegetation response to  
1157           climate changes projected by 8 GCMs. *Journal of Geophysical Research: Biogeosciences*,  
1158           113(G3). <https://doi.org/10.1029/2007JG000598>
- 1159   Bair E.H., Rittger K., Davis R.E., Painter T.H., Dozier J. (2016) Validating reconstruction of snow  
1160           water equivalent in California’s Sierra Nevada using measurements from the NASA  
1161           Airborne Snow Observatory *Water Resour. Res.*, 52 , pp. 8437-  
1162           8460, 10.1002/2016WR018704
- 1163   Bales, R. C., Molotch, N. P., Painter, T. H., Dettinger, M. D., Rice, R., & Dozier, J. (2006).  
1164           Mountain hydrology of the western United States. *Water Resources Research*, 42(8).  
1165           <https://doi.org/10.1029/2005WR004387>

1166 Barnett, T. P., Adam, J. C., & Lettenmaier, D. P. (2005). Potential impacts of a warming climate  
1167 on water availability in snow-dominated regions. *Nature*, 438(7066), 303–309.  
1168 <https://doi.org/10.1038/nature04141>

1169 Berghuijs, W. R., Woods, R. A., & Hrachowitz, M. (2014). A precipitation shift from snow  
1170 towards rain leads to a decrease in streamflow. *Nature Climate Change*, 4(7), 583–586.  
1171 <https://doi.org/10.1038/nclimate2246>

1172 Bixio, A. C., G. Gambolati, C. Paniconi, M. Putti, V. M. Shestopalov, V. N. Bublias, A. S.  
1173 Bohuslavsky, N. B. Kasteltseva, and Y. F. Rudenko (2002), Modeling groundwater-  
1174 surface water interactions including effects of morphogenetic depressions in the Chernobyl  
1175 exclusion zone, *Environ. Geol.*, 42(2-3) 162-177.

1176 Cayan, D. R., Maurer, E. P., Dettinger, M. D., Tyree, M., & Hayhoe, K. (2008). Climate change  
1177 scenarios for the California region. *Climatic Change*, 87(1), 21–42.  
1178 <https://doi.org/10.1007/s10584-007-9377-6>

1179 Christensen, L., Tague, C. L., & Baron, J. S. (2008). Spatial patterns of simulated transpiration  
1180 response to climate variability in a snow dominated mountain ecosystem. *Hydrological*  
1181 *Processes*, 22(18), 3576–3588. <https://doi.org/10.1002/hyp.6961>

1182 Collins, W. D., Bitz, C. M., Blackmon, M. L., Bonan, G. B., Bretherton, C. S., Carton, J. A., et al.  
1183 (2006). The Community Climate System Model Version 3 (CCSM3). *Journal of Climate*,  
1184 19(11), 2122–2143. <https://doi.org/10.1175/JCLI3761.1>

1185 Condon, L. E., Maxwell, R. M., & Gangopadhyay, S. (2013). The impact of subsurface  
1186 conceptualization on land energy fluxes. *Advances in Water Resources*, 60, 188–203.  
1187 <https://doi.org/10.1016/j.advwatres.2013.08.001>

1188 Condon, L.E., Atchley, A.L., Maxwell, R.M., (2020). Evapotranspiration depletes groundwater  
1189 under warming over the contiguous United States. *Nature Communications* 11, 873.  
1190 <https://doi.org/10.1038/s41467-020-14688-0>

1191 Cook, E. R., Woodhouse, C. A., Eakin, C. M., Meko, D. M., & Stahle, D. W. (2004). Long-Term  
1192 Aridity Changes in the Western United States. *Science*, 306(5698), 1015–1018.  
1193 <https://doi.org/10.1126/science.1102586>

1194 Coon, E. T., J. D. Moulton, and S. L. Painter (2016), Managing complexity in simulations of land  
1195 surface and near-surface processes, *Environ. Modell Software*, 78, 134-149.

1196 Cosgrove, B. A., Lohmann, D., Mitchell, K. E., Houser, P. R., Wood, E. F., Schaake, J. C., et al.  
1197 (2003). Real-time and retrospective forcing in the North American Land Data Assimilation  
1198 System (NLDAS) project. *Journal of Geophysical Research: Atmospheres*, 108(D22).  
1199 <https://doi.org/10.1029/2002JD003118>

1200 Cristea, N. C., Lundquist, J. D., Loheide, S. P., Lowry, C. S., & Moore, C. E. (2014). Modelling  
1201 how vegetation cover affects climate change impacts on streamflow timing and magnitude  
1202 in the snowmelt-dominated upper Tuolumne Basin, Sierra Nevada. *Hydrological*  
1203 *Processes*, 28(12), 3896–3918. <https://doi.org/10.1002/hyp.9909>

1204 Daly, C., Halbleib, M., Smith, J. I., Gibson, W. P., Doggett, M. K., Taylor, G. H., et al. (2008).  
1205 Physiographically sensitive mapping of climatological temperature and precipitation across the  
1206 conterminous United States. *International Journal of Climatology*, 28(15), 2031–2064.  
1207 <https://doi.org/10.1002/joc.1688>.

1208 Dettinger, M. (2011). Climate Change, Atmospheric Rivers, and Floods in California – A  
1209 Multimodel Analysis of Storm Frequency and Magnitude Changes<sup>1</sup>. *JAWRA Journal of*

1210 *the American Water Resources Association*, 47(3), 514–523.  
1211 <https://doi.org/10.1111/j.1752-1688.2011.00546.x>

1212 Dettinger, M., & Anderson, M. L. (2015). Storage in California’s reservoirs and snowpack in this  
1213 time of drought. *San Francisco Estuary and Watershed Science*, 13(2).  
1214 <https://doi.org/10.15447/sfews.2015v13iss2art1>

1215 Dettinger, M., Redmond, K., & Cayan, D. (2004). Winter Orographic Precipitation Ratios in the  
1216 Sierra Nevada—Large-Scale Atmospheric Circulations and Hydrologic Consequences.  
1217 *Journal of Hydrometeorology*, 5(6), 1102–1116. <https://doi.org/10.1175/JHM-390.1>

1218 Dettinger, M. D. (2013). Atmospheric Rivers as Drought Busters on the U.S. West Coast. *Journal*  
1219 *of Hydrometeorology*, 14(6), 1721–1732. <https://doi.org/10.1175/JHM-D-13-02.1>

1220 Di Liberto, T. (2017, October). Very wet 2017 WY ends in California. *NOAA Climate.Gov*.  
1221 Retrieved from [https://www.climate.gov/news-features/featured-images/very-wet-2017-](https://www.climate.gov/news-features/featured-images/very-wet-2017-water-year-ends-california)  
1222 [water-year-ends-california](https://www.climate.gov/news-features/featured-images/very-wet-2017-water-year-ends-california)

1223 Dierauer, J. R., Whitfield, P. H., & Allen, D. M. (2018). Climate Controls on Runoff and Low  
1224 Flows in Mountain Catchments of Western North America. *Water Resources Research*,  
1225 54(10), 7495–7510. <https://doi.org/10.1029/2018WR023087>

1226 Faunt, C.C., Belitz, K., Hanson, R.T., 2010. Development of a three-dimensional model of  
1227 sedimentary texture in valley-fill deposits of Central Valley, California, USA.  
1228 *Hydrogeology Journal* 18, 625–649. <https://doi.org/10.1007/s10040-009-0539-7>

1229 Faunt, C.C., Geological Survey (U.S.) (Eds.), 2009. Groundwater availability of the Central Valley  
1230 Aquifer, California, U.S. Geological Survey professional paper. U.S. Geological Survey,  
1231 Reston, Va.



1232 Ferguson, I. M. and Maxwell, R. M. (2010) Role of groundwater in watershed response and land  
1233 surface feedbacks under climate change, *Water Resour. Res.*, 46, 1–  
1234 15, <https://doi.org/10.1029/2009WR008616>.

1235 Ficklin, D. L., Luo, Y., & Zhang, M. (2013). Climate change sensitivity assessment of streamflow  
1236 and agricultural pollutant transport in California’s Central Valley using Latin hypercube  
1237 sampling. *Hydrological Processes*, 27(18), 2666–2675. <https://doi.org/10.1002/hyp.9386>

1238 Foster, L. M., Williams, K. H., & Maxwell, R. M. (2020). Resolution matters when modeling  
1239 climate change in headwaters of the Colorado River. *Environmental Research Letters*.  
1240 <https://doi.org/10.1088/1748-9326/aba77f>

1241 Gates WL (1992) AMIP: the atmospheric model intercomparison project. *Bull Am Meteorol Soc*  
1242 73(12):1962–1970. doi:10.1175/1520-0477(1992)073<1962:ATAMIP>2.0.CO;2

1243 Geologic Map of California, 2015. Geologic Map of California [WWW Document]. Geologic Map  
1244 of California. URL <https://maps.conservation.ca.gov/cgs/gmc/> (accessed 10.17.18).

1245 Gent, P. R., Danabasoglu, G., Donner, L. J., Holland, M. M., Hunke, E. C., Jayne, S. R., et al.  
1246 (2011). The Community Climate System Model Version 4. *Journal of Climate*, 24(19),  
1247 4973–4991. <https://doi.org/10.1175/2011JCLI4083.1>

1248 Gershunov, A., Shulgina, T., Clemesha, R.E.S. et al. (2019). Precipitation regime change in  
1249 Western North America: The role of Atmospheric Rivers. *Sci Rep* 9, 9944.  
1250 <https://doi.org/10.1038/s41598-019-46169-w>

1251 Gettelman, A., and Morrison, H. (2015). Advanced Two-Moment Bulk Microphysics for Global  
1252 Models. Part I: Off-Line Tests and Comparison with Other Schemes. *Journal of Climate*  
1253 28, 3, 1268-1287. <https://doi.org/10.1175/JCLI-D-14-00102.1>

1254 Gilbert, J.M., Maxwell, R.M., 2017. Examining regional groundwater - surface water dynamics  
1255 using an integrated hydrologic model of the San Joaquin River basin. *Hydrology and Earth*  
1256 *System Sciences* 21, 923–947. <https://doi.org/10.5194/hess-21-923-2017>

1257 Gleick, P. H. (1987). The development and testing of a water balance model for climate impact  
1258 assessment: Modeling the Sacramento Basin. *Water Resources Research*, 23(6), 1049–  
1259 1061. <https://doi.org/10.1029/WR023i006p01049>

1260 Godsey, S. E., Kirchner, J. W., & Tague, C. L. (2014). Effects of changes in winter snowpacks on  
1261 summer low flows: case studies in the Sierra Nevada, California, USA. *Hydrological*  
1262 *Processes*, 28(19), 5048–5064. <https://doi.org/10.1002/hyp.9943>

1263 Griffin, D., & Anchukaitis, K. J. (2014). How unusual is the 2012–2014 California drought?  
1264 *Geophysical Research Letters*, 41(24), 9017–9023.  
1265 <https://doi.org/10.1002/2014GL062433>

1266 Haarsma, R. J., Roberts, M. J., Vidale, P. L., Senior, C. A., Bellucci, A., Bao, Q., Chang, P., Corti,  
1267 S., Fučkar, N. S., Guemas, V., von Hardenberg, J., Hazeleger, W., Kodama, C., Koenigk,  
1268 T., Leung, L. R., Lu, J., Luo, J.-J., Mao, J., Mizielinski, M. S., Mizuta, R., Nobre, P., Satoh,  
1269 M., Scoccimarro, E., Semmler, T., Small, J., and von Storch, J.-S. (2016). High Resolution  
1270 Model Intercomparison Project (HighResMIP v1.0) for CMIP6, *Geosci. Model Dev.*, 9,  
1271 4185–4208, <https://doi.org/10.5194/gmd-9-4185-2016>.

1272 Harbaugh AW (2005) MODFLOW-2005, The U.S. Geological Survey modular ground-water  
1273 model: the ground-water flow process. US Geol Surv Tech Methods 6-  
1274 A16. <http://pubs.usgs.gov/tm/2005/tm6A16/>.

1275 Harpold, A. A., & Molotch, N. P. (2015). Sensitivity of soil water availability to changing  
1276 snowmelt timing in the western U.S. *Geophysical Research Letters*, *42*(19), 8011–8020.  
1277 <https://doi.org/10.1002/2015GL065855>

1278 Hayhoe, K., Cayan, D., Field, C. B., Frumhoff, P. C., Maurer, E. P., Miller, N. L., et al. (2004).  
1279 Emissions pathways, climate change, and impacts on California. *Proceedings of the*  
1280 *National Academy of Sciences*, *101*(34), 12422–12427.  
1281 <https://doi.org/10.1073/pnas.0404500101>

1282 He, M., Anderson, M., Schwarz, A., Das, T., Lynn, E., Anderson, J., et al. (2019). Potential  
1283 Changes in Runoff of California’s Major Water Supply Watersheds in the 21st Century.  
1284 *Water*, *11*(8), 1651. <https://doi.org/10.3390/w11081651>

1285 Herrington, A. R., P. H. Lauritzen, M. A. Taylor, S. Goldhaber, B. E. Eaton, J. T. Bacmeister, K.  
1286 A. Reed, and P. A. Ullrich (2019). Physics–Dynamics Coupling with Element-Based High-  
1287 Order Galerkin Methods: Quasi-Equal-Area Physics Grid. *Mon. Wea. Rev.*, *147*, 69–84,  
1288 <https://doi.org/10.1175/MWR-D-18-0136.1>.

1289 Homer, C., Dewitz, J., Yang, L., Jin, S., Danielson, P., Xian, G., et al. (2015). Completion of the  
1290 2011 National Land Cover Database for the conterminous United States—representing a  
1291 decade of land cover change information. *Photogrammetric Engineering & Remote*  
1292 *Sensing*, *81*(5), 345–354.

1293 Huang, X., Rhoades, A. M., Ullrich, P. A., & Zarzycki, C. M. (2016). An evaluation of the  
1294 variable-resolution CESM for modeling California’s climate. *Journal of Advances in*  
1295 *Modeling Earth Systems*, *8*(1), 345–369. <https://doi.org/10.1002/2015MS000559>

1296 Huang, X., Stevenson, S., & Hall, A. D. (2020). Future warming and intensification of  
1297 precipitation extremes: A “double whammy” leading to increasing flood risk in California.

1298 Geophysical Research Letters, 47, e2020GL088679.  
1299 <https://doi.org/10.1029/2020GL088679>

1300 Hurrell, J. W., Holland, M. M., Gent, P. R., Ghan, S., Kay, J. E., Kushner, P. J., et al. (2013). The  
1301 Community Earth System Model: A Framework for Collaborative Research. *Bulletin of*  
1302 *the American Meteorological Society*, 94(9), 1339–1360. [https://doi.org/10.1175/BAMS-](https://doi.org/10.1175/BAMS-D-12-00121.1)  
1303 [D-12-00121.1](https://doi.org/10.1175/BAMS-D-12-00121.1)

1304 Hurst. (1951) Long-Term Storage Capacity of Reservoirs, *Trans. Am. Soc. Civ. Eng.*, 116, 770–  
1305 799.

1306 Jones, P. W., (1999). First- and Second-Order Conservative Remapping Schemes for Grids in  
1307 Spherical Coordinates. *Mon. Wea. Rev.*, 127, 2204–2210, [https://doi.org/10.1175/1520-](https://doi.org/10.1175/1520-0493(1999)127<2204:FASOCR>2.0.CO;2)  
1308 [0493\(1999\)127<2204:FASOCR>2.0.CO;2](https://doi.org/10.1175/1520-0493(1999)127<2204:FASOCR>2.0.CO;2).

1309 IGBP, 2018. Global plant database published - IGBP [WWW Document]. URL  
1310 [http://www.igbp.net/news/news/news/globalplantdatabasepublished.5.1b8ae20512db692f](http://www.igbp.net/news/news/news/globalplantdatabasepublished.5.1b8ae20512db692f2a6800014762.html)  
1311 [2a6800014762.html](http://www.igbp.net/news/news/news/globalplantdatabasepublished.5.1b8ae20512db692f2a6800014762.html) (accessed 10.17.18).

1312 Jennings, C. W., Strand, R. G., & Rogers, T. H. (1977). Geologic map of California. Sacramento,  
1313 Calif.: Division of Mines and Geology.

1314 Kampenhout, L. van, Rhoades, A. M., Herrington, A. R., Zarzycki, C. M., Lenaerts, J. T. M.,  
1315 Sacks, W. J., & Broeke, M. R. van den. (2019). Regional grid refinement in an Earth system  
1316 model: impacts on the simulated Greenland surface mass balance. *The Cryosphere*, 13(6),  
1317 1547–1564. <https://doi.org/10.5194/tc-13-1547-2019>

1318 Kollet, S. J., & Maxwell, R. M. (2006). Integrated surface–groundwater flow modeling: A free-  
1319 surface overland flow boundary condition in a parallel groundwater flow model. *Advances*  
1320 *in Water Resources*, 29(7), 945–958. <https://doi.org/10.1016/j.advwatres.2005.08.006>

1321 Koutsoyiannis, D (2003) Climate change, the Hurst phenomenon, and hydrological statistics,  
1322 Hydrological Sciences Journal, 48:1, 3-24, DOI: 10.1623/ hysj.48.1.3.43481

1323 Koutsoyiannis, D., (2020) Revisiting the global hydrological cycle: is it intensifying?, Hydrology  
1324 and Earth System Sciences, 24, 3899–3932, doi:10.5194/hess-24-3899-2020.

1325 La Follette, P. T., Teuling, A. J., Addor, N., Clark, M., Jansen, K., & Melsen, L. A. (2021).  
1326 Numerical daemons of hydrological models are summoned by extreme precipitation.  
1327 Hydrology and Earth System Sciences, 25(10), 5425–5446. [https://doi.org/10.5194/hess-](https://doi.org/10.5194/hess-25-5425-2021)  
1328 [25-5425-2021](https://doi.org/10.5194/hess-25-5425-2021)

1329 Lehner, F., Deser, C., Maher, N., Marotzke, J., Fischer, E. M., Brunner, L., et al. (2020).  
1330 Partitioning climate projection uncertainty with multiple large ensembles and CMIP5/6.  
1331 Earth System Dynamics, 11(2), 491–508. <https://doi.org/10.5194/esd-11-491-2020>

1332 Lemordant, L., Gentine, P., Swann, A. S., Cook, B. I., & Scheff, J. (2018). Critical impact of  
1333 vegetation physiology on the continental hydrologic cycle in response to increasing CO2.  
1334 *Proceedings of the National Academy of Sciences*, 115(16), 4093–4098.  
1335 <https://doi.org/10.1073/pnas.1720712115>

1336 Liang, X., D. P. Lettenmaier, E. F. Wood, and S. J. Burges (1994), A simple hydrologically based  
1337 model of land surface water and energy fluxes for general circulation models, J. Geophys.  
1338 Res., 99(D7), 14415–14428, doi:10.1029/94JD00483.

1339 Lundquist, J. D., Hughes, M., Henn, B., Gutmann, E. D., Livneh, B., Dozier, J., & Neiman, P.  
1340 (2015). High-Elevation Precipitation Patterns: Using Snow Measurements to Assess Daily  
1341 Gridded Datasets across the Sierra Nevada, California, Journal of Hydrometeorology,  
1342 16(4), 1773-1792. doi: [https://journals.ametsoc.org/view/journals/hydr/16/4/jhm-d-15-](https://journals.ametsoc.org/view/journals/hydr/16/4/jhm-d-15-0019_1.xml)  
1343 [0019\\_1.xml](https://journals.ametsoc.org/view/journals/hydr/16/4/jhm-d-15-0019_1.xml)

1344 Maina, Fadji Z., Siirila-Woodburn, E. R., Newcomer, M., Xu, Z., & Steefel, C. (2020a).  
1345 Determining the impact of a severe dry to wet transition on watershed hydrodynamics in  
1346 California, USA with an integrated hydrologic model. *Journal of Hydrology*, 580, 124358.  
1347 <https://doi.org/10.1016/j.jhydrol.2019.124358>

1348 Maina, F. Z., Siirila-Woodburn, E. R., & Vahmani, P. (2020b). Sensitivity of meteorological-  
1349 forcing resolution on hydrologic variables. *Hydrology and Earth System Sciences*, 24(7),  
1350 3451–3474. <https://doi.org/10.5194/hess-24-3451-2020>

1351 Maina, Fadji Zaouna, & Siirila-Woodburn, E. R. (2020c). Watersheds dynamics following  
1352 wildfires: Nonlinear feedbacks and implications on hydrologic responses. *Hydrological*  
1353 *Processes*, 34(1), 33–50. <https://doi.org/10.1002/hyp.13568>

1354 Maina, Fadji Z., Siirila-Woodburn, E. R., & Denny-Frank, P. J. (2022) Assessing the impacts of  
1355 hydrodynamic parameter uncertainties on simulated evapotranspiration in a mountainous  
1356 watershed. *Journal of Hydrology* 608. <https://doi.org/10.1016/j.jhydrol.2022.127620>.

1357 Mallakpour, I., Sadegh, M., AghaKouchak, A., 2018. A new normal for streamflow in California  
1358 in a warming climate: Wetter wet seasons and drier dry seasons. *Journal of Hydrology* 567,  
1359 203–211. <https://doi.org/10.1016/j.jhydrol.2018.10.023>

1360 Maurer, E. P. (2007). Uncertainty in hydrologic impacts of climate change in the Sierra Nevada,  
1361 California, under two emissions scenarios. *Climatic Change*, 82(3), 309–325.  
1362 <https://doi.org/10.1007/s10584-006-9180-9>

1363 Maurer, E. P., & Duffy, P. B. (2005). Uncertainty in projections of streamflow changes due to  
1364 climate change in California. *Geophysical Research Letters*, 32(3).  
1365 <https://doi.org/10.1029/2004GL021462>

1366 Maxwell, R. M. (2013). A terrain-following grid transform and preconditioner for parallel, large-  
1367 scale, integrated hydrologic modeling. *Advances in Water Resources*, 53, 109–117.  
1368 <https://doi.org/10.1016/j.advwatres.2012.10.001>

1369 Maxwell, R. M., & Condon, L. E. (2016). Connections between groundwater flow and  
1370 transpiration partitioning. *Science*, 353(6297), 377–380.  
1371 <https://doi.org/10.1126/science.aaf7891>

1372 Maxwell, R. M., & Miller, N. L. (2005). Development of a Coupled Land Surface and  
1373 Groundwater Model. *Journal of Hydrometeorology*, 6(3), 233–247.  
1374 <https://doi.org/10.1175/JHM422.1>

1375 Mayer, T. D., & Naman, S. W. (2011). Streamflow Response to Climate as Influenced by Geology  
1376 and Elevation1. *JAWRA Journal of the American Water Resources Association*, 47(4),  
1377 724–738. <https://doi.org/10.1111/j.1752-1688.2011.00537.x>Boryan, C., Yang, Z.,  
1378 Mueller, R., Craig, M., 2011. Monitoring US agriculture: the US Department of  
1379 Agriculture, National Agricultural Statistics Service, Cropland Data Layer Program.  
1380 Geocarto International 26, 341–358. <https://doi.org/10.1080/10106049.2011.562309>

1381 Mallakpour, I., Sadegh, M., AghaKouchak, A., 2018. A new normal for streamflow in California  
1382 in a warming climate: Wetter wet seasons and drier dry seasons. *Journal of Hydrology* 567,  
1383 203–211. <https://doi.org/10.1016/j.jhydrol.2018.10.023>

1384 Maxwell, R.M., 2013. A terrain-following grid transform and preconditioner for parallel, large-  
1385 scale, integrated hydrologic modeling. *Advances in Water Resources* 53, 109–117.  
1386 <https://doi.org/10.1016/j.advwatres.2012.10.001>

1387 McEvoy, D.J., Pierce, D.W., Kalansky, J.F., Cayan, D.R., Abatzoglou, J.T., 2020. Projected  
1388 Changes in Reference Evapotranspiration in California and Nevada: Implications for

1389 Drought and Wildland Fire Danger. *Earth's Future* 8, e2020EF001736.  
1390 <https://doi.org/10.1029/2020EF001736>

1391 Milly, P. C. D., & Dunne, K. A. (2017). A Hydrologic Drying Bias in Water-Resource Impact  
1392 Analyses of Anthropogenic Climate Change. *JAWRA Journal of the American Water*  
1393 *Resources Association*, 53(4), 822–838. <https://doi.org/10.1111/1752-1688.12538>

1394 Milly, P. C. D., Dunne, K. A., & Vecchia, A. V. (2005). Global pattern of trends in streamflow  
1395 and water availability in a changing climate. *Nature*, 438(7066), 347–350.  
1396 <https://doi.org/10.1038/nature04312>

1397 Mote, P. W., Hamlet, A. F., Clark, M. P., & Lettenmaier, D. P. (2005). Declining mountain  
1398 snowpack in western north america\*. *Bulletin of the American Meteorological Society*,  
1399 86(1), 39–50. <https://doi.org/10.1175/BAMS-86-1-39>

1400 Musselman, K. N., Clark, M. P., Liu, C., Ikeda, K., & Rasmussen, R. (2017). Slower snowmelt in  
1401 a warmer world. *Nature Climate Change*, 7(3), 214–219.  
1402 <https://doi.org/10.1038/nclimate3225>

1403 Musselman, K. N., Molotch, N. P., & Margulis, S. A. (2017). Snowmelt response to simulated  
1404 warming across a large elevation gradient, southern Sierra Nevada, California. *The*  
1405 *Cryosphere*, 11(6), 2847–2866. <https://doi.org/10.5194/tc-11-2847-2017>

1406 National Operational Hydrologic Remote Sensing Center. (2004). Snow Data Assimilation  
1407 System (SNODAS) Data Products at NSIDC. <https://doi.org/10.7265/N5TB14TC>.

1408 Neelin, J. D., Langenbrunner, B., Meyerson, J. E., Hall, A., & Berg, N. (2013). California Winter  
1409 Precipitation Change under Global Warming in the Coupled Model Intercomparison  
1410 Project Phase 5 Ensemble. *Journal of Climate*, 26(17), 6238–6256.  
1411 <https://doi.org/10.1175/JCLI-D-12-00514.1>



1412 Neitsch, S. L., Arnold, J. G., Kiniry, J. R., & Williams, J. R. (2001). Soil and Water Assessment  
1413 tool (SWAT) user's manual version 2000. Grassland Soil and Water Research Laboratory.  
1414 Temple, TX: ARS.

1415 Niraula, R., Meixner, T., Dominguez, F., Bhattarai, N., Rodell, M., Ajami, H., et al. (2017). How  
1416 Might Recharge Change Under Projected Climate Change in the Western U.S.?  
1417 *Geophysical Research Letters*, 44(20), 10,407-10,418.  
1418 <https://doi.org/10.1002/2017GL075421>

1419 Niu, G.-Y., et al. (2011), The community Noah land surface model with multiparameterization  
1420 options (Noah-MP): 1. Model description and evaluation with local-scale measurements. *J.*  
1421 *Geophys. Res.*, 116, D12109, doi: 10.1029/2010JD015139.

1422 SMAP. (2015). Soil Moisture Active Passive. Retrieved October 18, 2018, from SMAP  
1423 website: <https://smap.jpl.nasa.gov/>

1424 Siirila-Woodburn, E. R., Rhoades, A. M., Hatchett, B. J., Huning, L. S., Szinai, J., Tague, C., Nico,  
1425 P. S., Feldman, D. R., Jones, A. D., Collins, W. D., and Kaatz, L.: A low-to-no snow future  
1426 and its impacts on water resources in the western United States, *Nature Reviews Earth and*  
1427 *Environment*, <https://doi.org/10.1038/s43017-021-00219-y>, 2021.

1428 Pascolini-Campbell, M., Reager, J. T., Chandanpurkar, H. A., & Rodell, M. (2021). A 10 per cent  
1429 increase in global land evapotranspiration from 2003 to 2019. *Nature*, 593(7860), 543–547.  
1430 <https://doi.org/10.1038/s41586-021-03503-5>

1431 Payne, A. E., Demory, M.-E., Leung, L. R., Ramos, A. M., Shields, C. A., Rutz, J. J., et al. (2020).  
1432 Responses and impacts of atmospheric rivers to climate change. *Nature Reviews Earth &*  
1433 *Environment*, 1(3), 143–157. <https://doi.org/10.1038/s43017-020-0030-5>

1434 Persad, G. G., Swain, D. L., Kouba, C., & Ortiz-Partida, J. P. (2020). Inter-model agreement on  
1435 projected shifts in California hydroclimate characteristics critical to water management.  
1436 *Climatic Change*, 162(3), 1493–1513. <https://doi.org/10.1007/s10584-020-02882-4>

1437 Ralph, F. M., & Dettinger, M. D. (2011). Storms, floods, and the science of atmospheric rivers.  
1438 *Eos, Transactions American Geophysical Union*, 92(32), 265–266.  
1439 <https://doi.org/10.1029/2011EO320001>

1440 Ralph, F. Martin, Neiman, P. J., Wick, G. A., Gutman, S. I., Dettinger, M. D., Cayan, D. R., &  
1441 White, A. B. (2006). Flooding on California’s Russian River: Role of atmospheric rivers.  
1442 *Geophysical Research Letters*, 33(13). <https://doi.org/10.1029/2006GL026689>

1443 Rasmussen, R., Liu, C., Ikeda, K., Gochis, D., Yates, D., Chen, F., et al. (2011). High-Resolution  
1444 Coupled Climate Runoff Simulations of Seasonal Snowfall over Colorado: A Process  
1445 Study of Current and Warmer Climate. *Journal of Climate*, 24(12), 3015–3048.  
1446 <https://doi.org/10.1175/2010JCLI3985.1>

1447 Rhoades, A. M., Huang, X., Ullrich, P. A., & Zarzycki, C. M. (2016). Characterizing Sierra Nevada  
1448 Snowpack Using Variable-Resolution CESM. *Journal of Applied Meteorology and*  
1449 *Climatology*, 55(1), 173–196. <https://doi.org/10.1175/JAMC-D-15-0156.1>

1450 Rhoades, A. M., Ullrich, P. A., & Zarzycki, C. M. (2018a). Projecting 21st century snowpack  
1451 trends in western USA mountains using variable-resolution CESM. *Climate Dynamics*,  
1452 50(1), 261–288. <https://doi.org/10.1007/s00382-017-3606-0>

1453 Rhoades, A. M., Jones, A. D., & Ullrich, P. A. (2018b). The changing character of the California  
1454 Sierra Nevada as a natural reservoir. *Geophysical Research Letters*, 45, 13,008– 13,019.  
1455 <https://doi.org/10.1029/2018GL080308>

1456 Rhoades, A. M., Ullrich, P. A., Zarzycki, C. M., Johansen, H., Margulis, S. A., Morrison, H., et  
1457 al. (2018c). Sensitivity of Mountain Hydroclimate Simulations in Variable-Resolution  
1458 CESM to Microphysics and Horizontal Resolution. *Journal of Advances in Modeling Earth*  
1459 *Systems*, 10(6), 1357–1380. <https://doi.org/10.1029/2018MS001326>

1460 Rhoades, A. M., Jones, A. D., O'Brien, T. A., O'Brien, J. P., Ullrich, P. A., & Zarzycki, C. M.  
1461 (2020a). Influences of North Pacific Ocean domain extent on the western U.S. winter  
1462 hydroclimatology in variable-resolution CESM. *Journal of Geophysical Research:*  
1463 *Atmospheres*, 125, e2019JD031977. <https://doi.org/10.1029/2019JD031977>

1464 Rhoades, A. M., Jones, A. D., Srivastava, A., Huang, H., O'Brien, T. A., Patricola, C. M., et al.  
1465 (2020b). The shifting scales of western U.S. landfalling atmospheric rivers under climate  
1466 change. *Geophysical Research Letters*, 47, e2020GL089096.  
1467 <https://doi.org/10.1029/2020GL089096>

1468 Rhoades, A. M., Risser, M. D., Stone, D. A., Wehner, M. F., & Jones, A. D. (2021). Implications  
1469 of warming on western United States landfalling atmospheric rivers and their flood  
1470 damages. *Weather and Climate Extremes*, 32, 100326,  
1471 <https://doi.org/10.1016/j.wace.2021.100326>

1472 Richards, L. A. (1931). Capillary conduction of liquids through porous medium. *Journal of*  
1473 *Applied Physics*, 1(5), 318–333. <https://doi.org/10.1063/1.1745010>

1474 Safeeq, M., Grant, G. E., Lewis, S. L., Kramer, M. G., & Staab, B. (2014). A hydrogeologic  
1475 framework for characterizing summer streamflow sensitivity to climate warming in the  
1476 Pacific Northwest, USA. *Hydrology and Earth System Sciences*, (18), 1–8.  
1477 <https://doi.org/10.5194/hess-18-3693-2014>

1478 Safeeq, M., Grant, G.E., Lewis, S.L. and Tague, C.L. (2013), Coupling snowpack and groundwater  
1479 dynamics to interpret historical streamflow trends in the western United States. *Hydrol.*  
1480 *Process.*, 27: 655-668. <https://doi.org/10.1002/hyp.9628>

1481 Safeeq, Mohammad, Grant, G. E., Lewis, S. L., & Staab, B. (2015). Predicting landscape  
1482 sensitivity to present and future floods in the Pacific Northwest, USA. *Hydrological*  
1483 *Processes*, 29(26), 5337–5353. <https://doi.org/10.1002/hyp.10553>

1484 SCRIPPS Institution of Oceanography. (2017, April). Northern California Just Surpassed the  
1485 Wettest Year on Record | Scripps Institution of Oceanography, UC San Diego. Retrieved  
1486 from <https://scripps.ucsd.edu/news/northern-california-just-surpassed-wettest-year-record>

1487 Shukla, S., Safeeq, M., AghaKouchak, A., Guan, K., & Funk, C. (2015). Temperature impacts on  
1488 the WY 2014 drought in California. *Geophysical Research Letters*, 4384–4393.  
1489 [https://doi.org/10.1002/2015GL063666@10.1002/\(ISSN\)1944-8007.CALDROUGHT1](https://doi.org/10.1002/2015GL063666@10.1002/(ISSN)1944-8007.CALDROUGHT1)

1490 Son, K., & Tague, C. (2019). Hydrologic responses to climate warming for a snow-dominated  
1491 watershed and a transient snow watershed in the California Sierra. *Ecohydrology*, 12(1),  
1492 e2053. <https://doi.org/10.1002/eco.2053>

1493 Song, X., Zhang, J., Zhan, C., Xuan, Y., Ye, M., Xu C., (2015) Global sensitivity analysis in  
1494 hydrological modeling: Review of concepts, methods, theoretical framework, and  
1495 applications. *Journal of Hydrology*, 523 pp. 739-757, 10.1016/j.jhydrol.2015.02.013

1496 Strachan, S., and Daly, C. (2017), Testing the daily PRISM air temperature model on semiarid  
1497 mountain slopes, *J. Geophys. Res. Atmos.*, 122, 5697– 5715, doi:10.1002/2016JD025920.

1498 Swain, D. L., Langenbrunner, B., Neelin, J. D., & Hall, A. (2018). Increasing precipitation  
1499 volatility in twenty-first-century California. *Nature Climate Change*, 8(5), 427–433.  
1500 <https://doi.org/10.1038/s41558-018-0140-y>

1501 Tague, C., & Peng, H. (2013). The sensitivity of forest water use to the timing of precipitation and  
1502 snowmelt recharge in the California Sierra: Implications for a warming climate. *Journal of*  
1503 *Geophysical Research: Biogeosciences*, 118(2), 875–887.  
1504 <https://doi.org/10.1002/jgrg.20073>

1505 Tang, G., Li, S., Yang, M., Xu, Z., Liu, Y., & Gu, H. (2019). Streamflow response to snow regime  
1506 shift associated with climate variability in four mountain watersheds in the US Great Basin.  
1507 *Journal of Hydrology*, 573, 255–266. <https://doi.org/10.1016/j.jhydrol.2019.03.021>

1508 The NCAR Command Language (Version 6.6.2) (2021). Boulder, Colorado:  
1509 UCAR/NCAR/CISL/TDD, 851 <http://dx.doi.org/10.5065/D6WD3XH5>.

1510 Trefry, M.G.; Muffels, C. (2007). "FEFLOW: a finite-element ground water flow and transport  
1511 modeling tool". *Ground Water*. 45 (5): 525–528. doi:10.1111/j.1745-6584.2007.00358.x

1512 Vicuna, S., & Dracup, J. A. (2007). The evolution of climate change impact studies on hydrology  
1513 and water resources in California. *Climatic Change*, 82(3), 327–350.  
1514 <https://doi.org/10.1007/s10584-006-9207-2>

1515 Vicuna, Sebastian, Maurer, E. P., Joyce, B., Dracup, J. A., & Purkey, D. (2007). The Sensitivity  
1516 of California Water Resources to Climate Change Scenarios1. *JAWRA Journal of the*  
1517 *American Water Resources Association*, 43(2), 482–498. [https://doi.org/10.1111/j.1752-](https://doi.org/10.1111/j.1752-1688.2007.00038.x)  
1518 [1688.2007.00038.x](https://doi.org/10.1111/j.1752-1688.2007.00038.x)

1519 Wang, S.-Y. S., Yoon, J.-H., Becker, E., & Gillies, R. (2017). California from drought to deluge.  
1520 *Nature Climate Change*, 7(7), 465. <https://doi.org/10.1038/nclimate3330>

1521 Welch, L.A., Allen, D.M., 2014. Hydraulic conductivity characteristics in mountains and  
1522 implications for conceptualizing bedrock groundwater flow. *Hydrogeol J* 22, 1003–1026.  
1523 <https://doi.org/10.1007/s10040-014-1121-5>

1524 Wu, C., Liu, X., Lin, Z., Rhoades, A. M., Ullrich, P. A., Zarzycki, C. M., et al. (2017). Exploring  
1525 a Variable-Resolution Approach for Simulating Regional Climate in the Rocky Mountain  
1526 Region Using the VR-CESM. *Journal of Geophysical Research: Atmospheres*, 122(20),  
1527 10,939-10,965. <https://doi.org/10.1002/2017JD027008>

1528 Zarzycki, C. M., Levy, M. N., Jablonowski, C., Overfelt, J. R., Taylor, M. A., and Ullrich, P. A.  
1529 (2014). Aquaplanet Experiments Using CAM's Variable-Resolution Dynamical Core.  
1530 *Journal of Climate* 27, 14, 5481-5503, <https://doi.org/10.1175/JCLI-D-14-00004.1>

1531

1532

1533

1534